

REPORT DOCUMENTATION PAGE

Form Approved

OMB No. 0704-0188

Public reporting burden for this collection of information is estimated to average 1 hour per response, including the time for reviewing instructions, searching existing data sources, gathering and maintaining the data needed, and completing and reviewing the collection of information. Send comments regarding this burden estimate or any other aspect of this collection of information, including suggestions for reducing this burden, to Washington Headquarters Services, Directorate for Information Operations and Reports, 1215 Jefferson Davis Highway, Suite 1204, Arlington, VA 22202-4302, and to the Office of Management and Budget, Paperwork Reduction Project (0704-0188), Washington, DC 20503.

1. AGENCY USE ONLY (Leave blank)		2. REPORT DATE September 12, 1997		3. REPORT TYPE AND DATES COVERED Final Technical Report	
4. TITLE AND SUBTITLE Cascade Arc Studies of Nonequilibrium Hydrogen/Nitrogen Plasma Propellants				5. FUNDING NUMBERS 9/15/95 - 9/14/97 F49620-94-1-0331 AFOSR-TR-97 0403	
6. AUTHOR(S) Dennis R. Keefer, PhD					
7. PERFORMING ORGANIZATION NAME(S) AND ADDRESS(ES) University of Tennessee Space Institute B.H. Goethert Parkway Tullahoma, Tn 37388				8. PERFORMING ORGANIZATION REPORT NUMBER	
9. SPONSORING / MONITORING AGENCY NAME(S) AND ADDRESS(ES) AFOSR/NA 110 Duncan Avenue, Suite B115 Bolling AFB, DC 20332-0001				10. SPONSORING / MONITORING AGENCY REPORT NUMBER	
11. SUPPLEMENTARY NOTES					
12a. DISTRIBUTION / AVAILABILITY STATEMENT Approved for public release; distribution is unlimited				12b. DISTRIBUTION CODE	
13. ABSTRACT (Maximum 200 words) A cascade arc facility was developed to study the characteristics of nonequilibrium plasma propellants for electric propulsion applications. The cascade arc was operated with hydrogen arcs at 2.0 and 6.0 psi. Spatially resolved spectral emission data were collected using a two dimensional Optical Multi-channel Analyzer (OMA). Electron density was determined by fitting theoretical line profiles to experimentally measured Abel inverted emissionline profiles. Radial distributions of plasma temperature also were estimated from Boltzmann plots of spectral line intensity. The measured electron number densities and plasma temperatures were compared to values predicted by nonequilibrium cascade arc simulations using the UTSI Cascade Arc Plasma Simulation (CAPS) code. The simulations underpredicted the peak experimental number densities by as much as an order of magnitude and over predicted peak plasma temperatures by as much as a factor of 2.5. The experimental electric field has been accurately predicted by varying chemical kinetics in the CAPS code. Kinetic models developed at the University of Illinois were found to give the best agreement with the Cascade Arc measurements. Electron number density profiles for simulated ammonia and hydrazine were also obtained at pressures of 2, 6 and 10 psi. Kinetic models for these mixtures will be evaluated when the CAPS code has been modified to simulate these propellants.					
14. Subject Terms Cascade Arc, Nonequilibrium plasmas, hydrogen, nitrogen, Spectroscopy, Stark effect				15. NUMBER OF PAGES 28	
				16. PRICE CODE	
17. SECURITY CLASSIFICATION OF REPORT Unclassified		18. SECURITY CLASSIFICATION OF THIS PAGE Unclassified		19. SECURITY CLASSIFICATION OF ABSTRACT Unclassified	
				20. LIMITATION OF ABSTRACT UL	

EXECUTIVE SUMMARY

A cascade arc facility has been constructed at The University of Tennessee Space Institute (UTSI) to study the effect of nonequilibrium transport properties in hydrogen-nitrogen arcjet propellant plasmas. The ability accurately to simulate arcjet flows has been limited by the lack of validated finite rate kinetic models and nonequilibrium transport properties. Measurements of plasma properties in the cascade arc are being used to guide development of the physical models required for further development of arcjet computational codes. The cascade arc has been operated on hydrogen with a current of 50 A at pressures of 2.0 psi and 6.0 psi. Spatially resolved spectral data at these conditions have been collected for the Balmer H_{α} , H_{β} , H_{γ} , and H_{δ} lines. The experimental H_{α} lineshapes have been fitted to theoretical lineshapes to determine the degree of Stark broadening. This allows the radial distributions of electron number density to be determined. Radial profiles of an equilibrium plasma temperature have also been estimated from Boltzmann plots using the line emission from H_{α} , H_{β} , H_{γ} , and H_{δ} lines. Candidate kinetic models were evaluated by comparing computer predictions using the UTSI Cascade Arc Plasma Simulation (CAPS) code with measurements of the plasma properties in the arc.

The CAPS code simulations have been run with a wide range of chemical kinetic models. The simulated plasma conditions were found to be extremely sensitive to the kinetic rates. The predicted nonequilibrium hydrogen plasma electron number densities underpredicted the experimental values by as much as an order of magnitude, and the peak electron densities were overpredicted by the equilibrium solutions. The experimentally measured values of the electric fields were bounded by the nonequilibrium computer simulations using different finite rate chemical kinetics. The finite rate chemical kinetic model closely matches the experimental electric field and best predicts the distribution of electron number densities. Boltzmann plots have been used to determine a rough estimate for the radial distribution of plasma electron temperature. These preliminary experimental temperature data are overpredicted by the simulations by as much as 2.5 times.

Cascade arc measurements have also been obtained for simulated ammonia and simulated hydrazine. Electron number density profiles have been obtained for 50 Amp arcs at 2 psi, 6 psi, and 10 psi. A hydrogen/nitrogen mixture version of the CAPS code is under development that will enable evaluation of candidate finite rate kinetic models for these important propellants.

Cumulative List of Professional Personnel:

Dennis Keefer
Trevor Moeller
Robert Rhodes
Newton Wright
Fred Schwartz
James Hornkohl
Thomas Walloschek

19971006 149

DTIC QUALITY INSPECTED 3

Publications:

T. Moeller, D. Keefer, and R. Rhodes, "Cascade Arc Studies of Nonequilibrium Hydrogen Plasmas," AIAA 96-3294, 32nd AIAA/ASME/SAE/ASEE Joint Propulsion Conference, Lake Buena Vista, FL, July 1-3, 1996.

T. Moeller, D. Keefer, and R. Rhodes, " Studies of Nonequilibrium Hydrogen/Nitrogen Plasmas using a Cascade Arc," AIP Conference Proceedings 387, p. 317, The Space Technology and Applications International Forum (STAIF-97), Albuquerque, NM, Jan. 1997.

T. Moeller, D. Keefer, and R. Rhodes, "Nonequilibrium Hydrogen/Nitrogen Plasmas Studies Using a Cascade Arc," IEPC 97-063, 25th International Electric Propulsion Conference, Cleveland, OH, August, 1997.

1.0 INTRODUCTION

Electric propulsion thrusters offer significant advantages for satellite station keeping and maneuvering, since their specific impulse can be more than twice that of conventional resistojets or chemical thrusters that are commonly used for these missions. Computational codes can be used to guide refinements in the configuration of electric propulsion thrusters that lead to better thruster performance. A number of computer simulation codes have been developed for this purpose[1-4]. However, it is now clear that there are important nonequilibrium processes in the propellant plasma that must be understood before adequate physical models can be constructed for use in these computational codes. A cascade arc facility has been constructed at The University of Tennessee Space Institute (UTSI) that permits accurate diagnostic measurements of nonequilibrium propellant plasma properties. These measurements are used to evaluate the kinetic models and transport properties required for further development of the computational codes.

1.1 USE OF THE CASCADE ARC FOR NONEQUILIBRIUM PLASMA RESEARCH.

Some of the most important chemical and transport processes in the propellant plasmas of electric propulsion thrusters, e.g. radial species diffusion and recombination, occur on time scales that are comparable to the convection times in these thrusters. This fast convection produces the strong axial gradients found in the propellant plasma. Therefore, the plasma conditions at a given point in a thruster depend strongly on the previous history of the plasma passing through that point. Comparison of code predictions with measurements in this case requires that the entire upstream flow field be accurately predicted. Differences between measured and predicted quantities could be due to inaccuracies in the models at any point upstream of the measurement location. This makes it very difficult to assess which model mechanisms or rates should be altered to improve the code.

Cascade arcs have long been used as a means to measure the fundamental atomic constants and transport properties of high temperature gases[5]. The cascade arc has a flow velocity much smaller than seen in electric propulsion thrusters, and the length of the arc plasma in the cascade is tens of diameters as compared to one diameter that is typical in electric propulsion devices. This produces plasmas with properties similar to propellant plasmas in electric propulsion thrusters but with negligible axial gradients. The radial temperature profiles in the cascade arc are controlled primarily by diffusive transport properties rather than convection. In the cascade arc, where there are no significant axial gradients, a balance between radial diffusion and chemical reactions with an axially constant but radially dependent energy input determines the nonequilibrium plasma parameters. The plasma properties depend on the local conditions at the measurement station rather than a complex space-time convolution of all the conditions upstream of the point of measurement. Differences observed between code predictions and measured quantities are more easily related to the specific reactions or diffusion rates which must be modified to improve the code models.

2.0 UTSI CASCADE ARC FACILITY

The UTSI cascade arc is comprised of individually water-cooled copper plates separated by electrical insulators (Figure 1). These plates are 3.175 mm (1/8 ") thick and form a 4 mm diameter arc channel that is approximately 40 mm long. The insulators are ceramic paper or mica 0.254 mm (0.010") thick. A modified water-cooled copper plate with windows allows optical access. This section is located in the center of the cascade arc to minimize end effects. The cathode is a 6.35 mm (0.250") diameter thoriated tungsten rod with a 60 degree cone on the end. The anode is 9.144 mm (0.360") diameter thoriated tungsten rod with a blunt end. A water jet impinging on their back surfaces cools both electrodes. The arc is driven by a 50 A, 600 V power supply. A cascaded centrifugal pump delivers 41.64 liters/min (11 gal/min) of water at 1.38 MPa (200 psi) to cool the copper plates and electrodes. The cascade arc is positioned vertically to eliminate arc asymmetries caused by buoyancy.

Accurate measurement of plasma parameters requires careful integration of the external optics with the design of the central window section. Abel inversion of the emission data is needed to provide radial measurements of the plasma properties[6]. Absolute emission measurements are necessary to determine species concentrations and provide a more accurate measurement of plasma temperatures. An adjustable, reflective Cassegrain optical collection system is used. to provide a small entrance solid angle for the cascade window section and to avoid off-axis aberrations. This collects light from the arc and directs it into a 1.25 meter focal length spectrometer so that the primary mirror in the spectrometer is overfilled (Figure 2). Figure 3 is a photograph of the UTSI Cascade Arc Facility. Before entering the Cassegrain telescope the light from the arc is rotated ninety degrees so that the radial dimension of the arc image lies along the slit. A two-dimensional optical multichannel analyzer (OMA) with image intensifier is used to collect and digitize the data. This detector has a 512 x 512 pixel detector array with 19 μm pixel spacing and is used to acquire simultaneous spectral data at many radial locations. The magnification of the optical system is approximately 1.0 providing 200 pixel resolution across the 4 mm diameter arc channel. Further details of the experimental setup were presented at the AIAA 32nd Joint Propulsion Conference[7].

3.0 EXPERIMENTAL PROCEDURE AND DATA REDUCTION

The cascade arc was operated with pure hydrogen arcs at 2.0 psi and 6.0 psi and a current of 50 A. Spectral emission data from the 656.28 nm Balmer alpha, H_{α} , line in the 8th order were collected using a 1.25 m Spex spectrometer with a 316 groove/mm echelle grating and a two-dimensional OMA detector[7]. Four images of the arc were collected at each pressure. A 1.9 N.D. filter and a 550 nm high-pass filter were utilized to prevent detector saturation and eliminate interference from higher order lines, respectively. The OMA detector exposure times were 0.2 seconds for the 6.0 psi case and 2.0 seconds for the 2.0 psi case. The 2.0 psi case required longer exposure times because the intensity of the radiation was lower. The images of the arc have 512 spectral pixels and 400 spatial pixels. Wavelength calibration was performed on the spectral pixels using seven lines from a low-density neon calibration source. The spatial pixels were calibrated by taking images of a 50 μm vertical slit backlit by the neon lamp and placed in the same position as the arc when the cascade is in operation. By moving the vertical

slit across the location of the arc with a precision translation table, the spatial pixels were associated with a radial position across the arc region. The spectrometer slit function was experimentally measured using a narrow neon spectral line, and the measured spectral lines were spectrally deconvolved using a digital Wiener filter[8].

Because the Stark effect has strong dependence on electron number densities and depends only slightly on temperature, the electron number density of a plasma can be determined independently of the plasma temperature by comparing theoretical line widths to the experimentally measured H_{α} lines [6]. The 2-D OMA captures spectral intensity data at many spatial locations across the arc simultaneously. Because this intensity data is a line-of-sight projection of the emission data onto a one-dimensional plane, it must be Abel inverted to obtain radial profiles of the spectral emission. Theoretical line widths can then be compared to this radial distribution of spectral lines to determine the radial variation of electron number density.

The Abel inversion is performed using a modern approach that utilizes integral transforms [10]. In this method, the Abel inversion of line-of-sight intensity data into radially distributed emission data is accomplished by taking the Fourier transform of the intensity data and then performing an inverse Hankel transform. A method for determining the center of the data is incorporated in this inversion technique that minimizes asymmetries. Because Abel inversion implies radial symmetry, any asymmetry is assumed to be noise. Since the Fourier transform of symmetric data is real and the Fourier transform of asymmetric data has imaginary components, the imaginary components of asymmetric data are noise, by definition. Therefore, by shifting the data so that the imaginary components of the transform are minimized, the center can be found. Because fast Fourier transforms (FFT's) can be implemented in the method described above, this Abel inversion process can be performed much faster than conventional methods.

The following algorithm has been used to implement this Abel inversion approach in our data analysis. (1) A fast Fourier transform (FFT) is performed on the intensity data. (2) High frequency noise is filtered out of spectral data using an optimal, finite impulse response (FIR), low band pass filter. (3) The inverse fast Fourier transform (IFFT) is performed on the data. These first three steps smooth the spectral data by filtering out high frequency noise. The Abel inversion is performed next. (4) Perform FFT on spatial data. (5) Filter spatial high frequency noise using another FIR, low band pass filter. (6) Center transformed data by shifting to minimize imaginary component of transformed data. (7) Discard the imaginary part of the shifted, transformed data. This step eliminates noise (asymmetries) in the data. (8) Perform the inverse Hankel transform to obtain the Abel inverted data.

After Abel inversion, a radial distribution of broadened emission profiles is obtained. At the pressures tested, both Doppler and Stark effects broaden the lines. The resulting line profile is a Voigt profile--a convolution of Gaussian (Doppler) and Lorentzian (Stark) lineshapes. A downhill simplex computer algorithm [11] was used to fit a Voigt profile to the experimental data. From this fitting routine, line widths for both the Lorentzian and Gaussian components of the Voigt profile were determined. Plasma line broadening theory was used to correlate the width of the Stark component to the electron number density. Broadening due to the Stark effect has been calculated using two assumptions about ion motion [6,12]. The first assumption states

that the ions have a very small velocity compared to the electrons. This assumption implies that the broadening due to atomic collisions with ions is insignificant compared broadening due to the atomic collisions with electrons. The second assumption relaxes the stationary ion restriction, and therefore includes excitation of atoms through collisions with moving ions. In general, the dynamic ion assumption results in significantly broader line widths for the same electron number density [12] and should be included.

To obtain estimates of plasma electron temperature distributions in the 50 A hydrogen arcs at 2 psi and 6 psi, emission profiles of the H_{α} , H_{β} , H_{γ} , and H_{δ} lines were used to make radially resolved Boltzmann plots. The emission profiles were obtained using the Abel inversion technique described above. This data was collected in the second order to guarantee an accurate estimate of the continuum. A standard tungsten filament lamp was used to calibrate the spectral sensitivity of the detector over the range defined by these spectral lines.

Further details of the experimental procedure were presented at the AIAA 32nd Joint Propulsion Conference[7] , the 1st Conference on Synergistic Power and Propulsion Systems Technology[9], and the 25th International Electric Propulsion Conference [13]. This experiment has been repeated for simulated ammonia and simulated hydrazine at pressures of 2 psi, 6 psi, and 10 psi. Detector exposure times of 2 seconds were used for these measurements. Results are shown in Sections 5 and 6.

4.0 THE UTSI CASCADE ARC PLASMA SIMULATION (CAPS) CODE

The equilibrium and nonequilibrium UTSI arcjet computer codes have been modified into one-dimensional nonequilibrium and equilibrium Cascade Arc Plasma Simulation (CAPS) codes[14]. At present these codes model a H_2 , H , H^+ , e hydrogen system. Both codes include radiation transport. The nonequilibrium version includes species diffusion and a finite rate chemistry kinetic model and uses a two-temperature model with separate energy equations for heavy species and electrons. In both codes it is assumed that the pressure is constant, the radial velocity is zero, and the radial current density is zero. The required mass flow is assured by adjustment of velocity levels. The consequence of these assumptions is that species production and diffusion are locally balanced and total production is balanced by wall losses for the axial momentum, energy, electron energy, and species. The transport properties for both the equilibrium and nonequilibrium versions of the UTSI cascade arc computer code are calculated using a computer code written by Cho based on the procedures developed by DeVoto[15].

4.1 The Numeric Model and Governing Equations

The algorithm for the solution of the governing equations in the CAPS code is the same as that used in the UTSI arcjet simulation code [14]; however, the CAPS code assumptions mentioned above greatly simplify the governing equations. These governing equations are discussed in this section. The algorithm for the CAPS code is a Navier-Stokes solver based on the SIMPLE (Semi-implicit Pressure Linked Equation) algorithm developed by Gosman and Pun [16] and modified by Rhie [17] to accommodate both supersonic and subsonic flow. Jeng [18, 19] and

Rhodes [20] incorporated a magnetic field equation coupled with heat release to study laser heat addition and radio frequency heating of a plasma, respectively. The code is formulated to solve the steady-state Navier-Stokes equations. The governing equations in the code are solved in a transformed coordinate where the original, non-orthogonal, axially symmetric grid is mapped to a grid of unit squares [21].

The computation grid representing the UTSI Cascade Arc is shown in Figure 4. The axial dimension is along the abscissa and the radial dimension is along the ordinate. The grid point density increases near the wall to aid code convergence in regions where radial gradients can be large. The CAPS code uses the program control and array structure used in the UTSI arcjet simulation code. As a result, the CAPS code computation grid has an axial dimension, even though conservation equations are solved only in the radial direction. The conservation equations are solved for grid cells in the transformed computation grid (see Figure 5).

The SIMPLE algorithm used in the CAPS code is a solver for equations of the form:

$$\nabla \cdot \rho \bar{v} \phi = \nabla \cdot \Gamma_{\phi} \nabla \phi + S \quad (1)$$

where ϕ represents the axial velocity (u), the static enthalpy (H), the electron temperature (T_e for nonequilibrium), and species concentrations (α_i for nonequilibrium). Γ represents the transport coefficient appropriate for each variable. Any terms that cannot be put into a convective or diffusive form are added to the source term, S . The transformation of the grid coordinates into a grid of unit squares results in mixed derivatives from diffusive terms that are also added to S [14]. Second order accurate finite difference representations are used to represent equation (1) for the variable under consideration at each point in the computation grid. Written in matrix form, these coupled equations result in a tri-diagonal matrix that is solved using a tri-diagonal solver. Equation (1) is solved for each of the dependent variables using under-relaxation. Updated values of the dependent variables are used when they are available, and old values are used when the variables have yet to be updated. The process of solving equation (1) for each of the dependent variables is repeated until the sum of the all of the residual errors has reduced to an acceptably small value [14]. At this point the numerical solution to the problem is no longer changing significantly.

4.1.1 Equilibrium/Nonequilibrium Momentum Equation

The form of the momentum conservation equation is the same for both the equilibrium and nonequilibrium cases. The axial velocities are obtained from the momentum equation for steady, axially symmetric flow [21]. The momentum equation in vector form is [22]

$$\nabla \cdot \rho \bar{v} \cdot \bar{v} = \nabla \cdot \mu \nabla \bar{v} - \nabla p - \nabla \times (\mu \nabla \times \bar{v}) + \mathbf{J} \times \mathbf{B} \quad (2)$$

Where ρ is the density, \bar{v} is the velocity of the gas (\bar{v} is equal to the axial velocity), p is the pressure, μ is the viscosity, \mathbf{J} is the current density, which only has an axial component, and \mathbf{B} is

the magnetic field. Because of the constant pressure assumption, the pressure force term, $-\nabla p$, is zero. The Lorentz body force term, $\mathbf{J} \times \mathbf{B}$, is indirectly zero because of assumptions in the code. Since the current has only an axial component and the magnetic field only has an azimuthal component, the cross product of \mathbf{J} and \mathbf{B} is in the radial direction. The flow in the cascade is assumed to be axial; therefore, the Lorentz force in the radial direction has no effect on the momentum equation (only the axial momentum equation is solved in this problem). The momentum equation solved in the CAPS code is

$$\nabla \cdot \rho \bar{v} \cdot \bar{v} = \nabla \cdot \mu \nabla \bar{v} - \nabla \times (\mu \nabla \times \bar{v}) \quad (3)$$

As mentioned above, the momentum equation is the same for both the equilibrium and the nonequilibrium versions of the code.

4.1.2 Equilibrium Energy Equation

The equilibrium CAPS code assumes local thermodynamic equilibrium (LTE). This assumption implies that the temperature of all of the particles in the gas is the same. Therefore, only one energy equation is necessary to describe a plasma in LTE. The static enthalpy, H , is obtained from the following energy equation, which includes ohmic heating, radiation loss, and viscous dissipation [22].

$$\nabla \cdot \rho \bar{v} H = \nabla \cdot \frac{k}{C_p} \nabla H + \Phi + q_i - q_r + \bar{v} \cdot \nabla p \quad (4)$$

where

$$\begin{aligned} \Phi &= \text{viscous dissipation,} \\ \Phi &= \mu \left[2 \left(\frac{\partial u}{\partial x} \right)^2 + \left(\frac{\partial u}{\partial r} \right)^2 - \frac{2}{3} \left(\frac{\partial u}{\partial x} \right)^2 \right] \end{aligned} \quad (5)$$

and

c_p = specific heat
 k = thermal conductivity
 q_i = ohmic heating = $(J_x^2 + J_r^2)/\sigma$
 q_r = radiation loss
 r = radius
 μ = viscosity
 ρ = gas density.

Because pressure is assumed to be constant, the last term in equation (4) is zero. The calculation of the thermodynamic properties and equilibrium transport properties will be discussed in section 4.3.

4.1.3 Nonequilibrium Energy Equation

Several choices are available for the form of the two energy equations necessary to describe a two-temperature nonequilibrium plasma. In this work, energy equations for the electron energy and the static energy of the whole mixture are used. These equations were chosen because the form of the energy balance for the whole mixture is the same as that for the equilibrium case [14].

Because the nonequilibrium CAPS code relaxes the LTE assumption, the temperature of the electrons is not necessarily equal to the temperature of the heavy particles. The energy distribution of the heavy particles and the electrons are assumed to be Boltzmann distributions at the heavy particle temperature and electron temperature, respectively. Therefore, the energy in the system must be represented by two energy equations. The equation for the mixture enthalpy, H , is [14]

$$\nabla \cdot \rho \bar{v} H = \nabla \cdot \left[\frac{k}{C_{ph}} \nabla H + \left(\rho D - \frac{k}{C_{ph}} \right) \sum h_i \nabla \alpha_i - k \alpha_e \frac{C_{pe}}{C_{ph}} \nabla T_e \right] \quad (6)$$

$$+ \Phi + q_i - q_r + \bar{v} \cdot \nabla p$$

where

k = thermal conductivity of the mixture

$C_{ph} = \sum \alpha_i h_i$ = specific heat of heavy particles

where the summation includes the heavy particles.

C_{pe} = specific heat of electrons

D = mixture diffusion coefficient [14]

α_i = concentration of plasma constituent 'i'

T_e = electron temperature.

The last term in equation (6) is zero because of the constant pressure assumption. Equation (6) is one of the energy equations required to represent the two-temperature system modeled in the nonequilibrium CAPS code.

An equation representing the energy in the electron gas is the other equation chosen to represent the energy in the two-temperature system. In this equation, electron conduction, convection, diffusion, and energy transport to the heavy particles through collision [14] balances the electrical Ohmic heating. The form of the equation is taken from Park [23].

$$\nabla \cdot \rho \bar{v} \alpha_e h_e - \nabla \cdot [k_e \nabla T_e + h_e D \nabla \alpha_e] - \bar{v} \cdot \nabla p_e = S \quad (7)$$

where $S = q_{ce} + q_{ch} + q_i - q_r$. The last term on the left-hand side of equation (7) describes the work done by the electron-pressure gradients. This term is zero because of the constant pressure assumption.

"The term q_{ce} represents the transfer of energy between the heavy gas and the electron gas resulting from collisions of electrons with heavy species," [14]

$$q_{ce} = \sum_i^{h.p.} 2n_e \frac{m_e}{m_i} v_i \frac{3}{2} k(T - T_e) \quad (8)$$

where the summation is over the species in the heavy gas. The collision frequency is evaluated from the temperature dependent collision cross-sections for electron-heavy collisions evaluated at the electron temperature using the transport property [routines] described in section 4.3. [14]

Energy transport to the electron gas due to electron participation in chemical reactions is represented by the term, q_{ch} , in equation (7). The energy released by a three body recombination reaction with the electron acting as the third body is assumed to be absorbed into the electron gas, raising the electron temperature. Ionization and dissociation due to electron collision is assumed to remove the dissociation or ionization energy from the electron gas, lowering the electron temperature [14].

The electrical energy input to the system, q_j , is the same Ohmic heating (J^2/σ) used in the equilibrium simulation. The thermodynamic and nonequilibrium transport properties are discussed in section 4.3.

4.2 Boundary Conditions

The radial gradients of u , H , h_e (in the nonequilibrium case), and p are set equal to zero on the symmetry axis (centerline). A no-slip condition is forced by specifying that the axial velocity is zero at the wall. The axial velocity is calculated from the pressure and the density and is adjusted to ensure the required mass flow. The wall has a specified temperature and is assumed to be catalytic for electron-ion recombination and hydrogen atom recombination. This results in an equilibrium condition at the wall with the gas enthalpy specified by the pressure and the wall temperature. This equilibrium condition at the wall is true in the nonequilibrium plasma as well as the equilibrium plasma [14].

4.3 Species

Because the equilibrium CAPS code assumes LTE and chemical equilibrium, species concentrations are a function of pressure and temperature. These concentrations are defined by the Saha equation [6], a form of the law of mass action, which assumes all chemical reactions have equilibrated. The Saha equation cannot be used to obtain nonequilibrium species concentrations since the time scales are too short for chemical reactions to be complete. For this case, finite rate chemical kinetics must be included in the CAPS code model.

For the nonequilibrium CAPS code, the system of governing equations (Section 4.1) are expanded to include three species equations and allow the calculation of systems where ionization of H and the dissociation of H_2 are not in equilibrium [14]. The hydrogen system is modeled as a four component system: molecular hydrogen, H_2 ; atomic hydrogen, H ; hydrogen

ion, H^+ ; and electrons, e . Because the system is electrically neutral, the electrons and hydrogen ions can be represented by the same species conservation equation (this allows the four species system to be modeled by three species concentration equations). The species conservation equation used in the CAPS code is [14]

$$\nabla \cdot \rho \vec{v} \alpha = \nabla \cdot \rho D \nabla \alpha + S_\alpha \quad (9)$$

where α is the species under consideration, and S_α is the production of the species by chemical reaction. The source term (S_α) is equal to the change in species concentration divided by a chemical time step. This chemical time step is calculated from the mass in the computation cell of interest divided by the mass flux into the cell [14]. The species conservation equations (equation 9) are then solved over the chemical time step using a linearized set of equations for the four hydrogen species [24].

The species production needed in the above calculation are calculated from chemical kinetic reaction rate coefficients. The forward reaction rate coefficients are calculated from the Arrhenius equation [25]

$$k_f = AT^{-n} e^{(E/RT)} \quad (10)$$

where

- A = Arrhenius constant
- E = activation energy
- R = universal gas constant
- T = temperature.

The Arrhenius constant, the activation energy, and the power of the temperature, n , are user input to the computer program. The backward kinetic reaction rate coefficients, k_b , are calculated from k_f and the equilibrium constant, K_p [25].

$$k_b = -\frac{k_f}{K_p} \quad (11)$$

The calculated reaction rates can vary greatly for a chemical reaction depending on the kinetic rate constants used in equation (10). The species concentrations obtained from the computer simulations are extremely sensitive to the calculated rate constants.

Furthermore, a significant amount of the energy is transported between the electrons and the heavy species when an electron acts as the third body in a reactive collision [7]. As a result, the recombination reaction rates can influence the electron to heavy gas temperature ratio, as well as the gas composition. The reaction rates for the hydrogen system used in the computer simulations in this work is presented in Table 1.

4.4 Transport Properties

The transport properties for both the equilibrium and nonequilibrium versions of the UTSI cascade arc computer code are calculated using a computer code written by Cho [15] based on the procedures developed by DeVoto [26]. The transport property models used in this reference are based on the Chapman-Enskog method [27, 28]. The models in Cho's code start with experimental or calculated energy dependent collision cross-sections, calculate the collision integrals based on one of several interaction models and use combinations of the collision integrals to determine the transport properties. Electrical conductivity and electron thermal conductivity depend on collisions between electrons and heavy species in the mixture, while viscosity and heavy gas thermal conductivity depend primarily on collisions between the heavy species [7].

The Cho model makes the following assumptions when used with a two-temperature nonequilibrium plasma model. The fundamental cross-section data describes the interaction of one atom or molecule with another, and depends only upon collision energy and the identity of the colliding pair. The nonequilibrium plasma is described by a two-temperature model where a Maxwellian distribution at a unique electron temperature describes the kinetic energy of the electrons. The electron temperature is used to determine the collision energy for all collisions involving electrons, since the relative velocity of a collision involving an electron is close to the velocity of the electron. The heavy gas temperature is used to determine the collision energy for all other collisions [7].

Radiation transport is calculated using the methods described by Griem [6] that include both line and continuum emission. Energy transport through radiation is modeled as having an optically thin part and an optically thick part. The optically thin radiation is not absorbed back into the plasma gas and is assumed to result in a direct energy loss from the plasma to the constrictor wall of the cascade arc. The optically thick component is absorbed back into the plasma gas and is modeled as a thermal conductivity using the Rosseland approximation [29]. This Rosseland thermal conductivity is fitted as a function of mixture enthalpy, electron concentration, and pressure for a hydrogen plasma in equilibrium. The resulting equation is used in nonequilibrium code [14]. Any error associated with this assumption is assumed to be small because optically thick radiation is very small when compared to the other energy transport mechanisms in hydrogen plasmas at pressures and temperatures realized in the UTSI cascade arc. The Rosseland thermal conductivity is added to the internal thermal conductivity of the heavy species to form an effective thermal conductivity for use in the CAPS code. The Rosseland component is not added to the electron thermal conductivity. Simulations of the UTSI Cascade Arc running on hydrogen have been performed using the CAPS code. Results from these simulations and comparisons with experimental results are presented in Sections 5 and 6.

5.0 COMPARISON OF EXPERIMENTAL AND NUMERICAL RESULTS FOR HYDROGEN

The cascade arc was operated with pure hydrogen arcs at 2.0 psi and 6.0 psi and a current of 50 Amperes. Several different sets of data were taken at each condition and the data was analyzed using the methods described in Section 3. The spatial FIR smoothing filter used in the Abel inversion algorithm had a cutoff frequency of 4 percent of the Nyquist frequency while the spectral filter had a cut off frequency of 20 percent and 6 percent of Nyquist frequency for the 2 psi and 6 psi cases, respectively. A typical Abel inverted line profile at 6.0 psi and a radius of 1.5 mm and its Voigt fit are shown in Figure 6. This shows the good agreement between experimentally determined profiles and the Voigt lineshapes. The radial profile of the integrated emission data for the 6.0 psi case is shown in Figure 7. The error bars on the emission of plus or minus one standard deviation of the output noise are estimates of the error associated with the Abel inversion. This error was calculated from the variance of the input noise and the spatial bandpass cutoff frequency using a method developed by Smith [29]. Smith shows that "the variance of the output noise is directly proportional to the variance of the input noise and to the bandwidth [of the filter], and inversely proportional to the radial distance from the origin" [29]. As can be seen in Figure 7, the error is inversely proportional to the radius. The error asymptotically approaches infinity as the radius goes to zero. However, when the radius is as little as 20 μm , the standard deviation of the emission has decreased to a few percent of the emission and continues to decrease with radius. The emission has not decreased to zero at 2 mm, the radius of the arc constrictor. A possible explanation for this feature is that the plasma might be slightly bowed into the optical channels leading to the windows

The reaction rates for the hydrogen system used in the computer simulations are shown in Table 1. The "slow" and "fast" rates, presented at the 25th AIAA Plasmadynamics and Lasers Conference[2], have different chemical kinetic rates for the three-body ionization and recombination of hydrogen atoms by electrons. The "U of I" (University of Illinois) rates presented at the 26th AIAA Plasmadynamics and Lasers Conference[1] are the same as the "fast" rates but have a different rate for the dissociation of molecular hydrogen by electrons[31]. The forward reaction rates in Table 1 are given by $k_f = a/T^n \exp(E/RT)$. T is the electron temperature for reactions 3, 3 U of I, 5, 5r, and 5i; and M is any third body. Reaction 5r is the slow recombination rate, and 5i is the slow ionization rate.

Comparisons of the radial distribution of calculated and experimental electron number densities for the 2.0 psi and 6.0 psi cases are presented in Figures 8 and 9, respectively. The same cascade arc data were analyzed using two different Stark broadening models, one that assumes static ions and the other that assumes dynamic ions. The results yielded by each assumption are labeled 'static' and 'dynamic'. The computer simulations were run using the three sets of finite chemical kinetic rates (Table 1). The error bars on the experimental electron number densities (Figures 8 and 9) are plus or minus one standard deviation of the four realizations at each pressure. At 6.0 psi, the nonequilibrium computer simulations underpredict the experimentally determined electron number densities for both the static and dynamic ion assumptions at all radii and for all ionization rates. At 2.0 psi, the experimental electron number densities are underpredicted by all of the simulations when using the static ion assumption. However, the

experimental electron number densities are bounded by the simulated nonequilibrium electron number densities for the dynamic ion assumption. While the 'dynamic' electron number densities are underpredicted by about an order of magnitude for the "slow" cases, the results for the "fast" case reduce this underprediction to about a factor of two at 6.0 psi and an overprediction of about 20 percent at 2.0 psi. The "U of I" case gives the best nonequilibrium solution results; it underpredicts the 6.0 psi experimental values by less than a factor of three on centerline and matches the experimental value at 2.0 psi. The equilibrium simulation predicts that the electron number density becomes negligible at a radius of 1.5 mm while the nonequilibrium simulations predict significant electron densities all the way to the wall. This characteristic is also clearly seen in the data.

Figures 10 and 11 show comparisons of the radial distribution of calculated and experimental electron temperatures for the 2.0 psi and 6.0 psi cases, respectively. Only the "U of I" nonequilibrium solutions are presented in these plots for the sake of brevity. The computer simulations overpredict the experimental centerline temperatures by approximately 60 percent for the 2.0 psi case and match the experiment (within experimental error) for the 6.0 psi case. The measured temperature profiles do not match any of simulation temperature distributions. The negative temperature gradient at the constrictor wall and the 50 percent error of the experimental temperature distributions make these preliminary data questionable. The error bars on the experimental data are plus or minus one standard deviation calculated from the uncertainty associated with the slope of the line in the Boltzmann plot (the Boltzmann plot of a 6 psi hydrogen arc is shown in Figure 12). The relatively large error in temperature results from poor fits through the four data points in the Boltzmann plots.

Table 2 is a comparison of the experimental and numerical electric field for the 2.0 psi and 6.0 psi cases. The experimental electric fields were determined by finding the slope of the best fit line through the measured potentials of the cascade plates. The electric fields from the equilibrium simulations overpredict the experimentally determined values by 33 percent for the 2.0 psi case and 10 percent for the 6.0 psi case. These overpredictions increase to 180 percent and 51 percent for the "slow" nonequilibrium simulations at 2.0 psi and 6.0 psi, respectively. The electric field for the "fast" nonequilibrium simulations overpredicts the experiment by 17 percent for 2.0 psi and agrees with the value for 6.0 psi. The "U of I" nonequilibrium simulations best predict the electric field, splitting the experimental values for the 2.0 psi case and matching the values for the 6.0 psi case. It is evident that the chemical kinetic rates have a large impact on the electric field realized in the nonequilibrium computer simulations.

6.0 RESULTS FOR HYDROGEN/NITROGEN PLASMAS

The cascade arc was also operated on simulated ammonia and hydrazine at 2.0, 6.0, and 10.0 psi and 50 Amps. The radial distribution of experimental electron number densities for simulated ammonia and simulated hydrazine are shown in Figures 13 and 14, respectively. These data show an increase in electron density with pressure, and a very slight increase in electron density for the hydrazine over the ammonia. An interesting feature of the profiles is the positive slope of the curve close to the wall of the arc channel at 2 mm. This feature can be explained by a combination of two factors, both magnified by a low signal level at these larger radii. First, some

of the light from the broader lines near the arc center can reflect off of the optical channels so that it appears to be originating closer to the walls. This reflected light effectively broadens the thinner and weaker line emission near the walls. Second, it is very difficult to determine the exact magnitude of the continuum. A small increase in the background level can cause artificial broadening in the Abel inversion technique. Filtering of the signal noise for the mixture data has not yet been optimized and may also be contributing to this problem. Table 3 shows a comparison of experimentally determined electric fields for the hydrogen and hydrogen/nitrogen mixtures. The electric field increases with pressure and decreases as more nitrogen is added.

7.0 CONCLUSIONS

Nonequilibrium plasma conditions of 50 Amp hydrogen arcs at 2.0 and 6.0 psi have been measured and compared with computer simulations using the UTSI CAPS code. The simulations have been run with a wide range of chemical kinetics. The simulated plasma conditions were found to be extremely sensitive to the kinetics. The predicted nonequilibrium hydrogen plasma electron number densities underpredicted the experimental values (using the dynamic ion assumption) by as much as an order of magnitude, and the peak electron densities were overpredicted by the equilibrium solutions. The experimental electric fields can be bounded by the nonequilibrium computer simulations by using different finite rate chemical kinetic rates. The "U of I" finite rate chemical kinetic model matches the experimental electric field and best predicts the distribution of electron number densities. In addition to the measured distributions of electron number densities, Boltzmann plots have been used to determine a rough estimate for the radial distribution of plasma electron temperature. These preliminary experimental temperature data are overpredicted by the simulations by as much as 2.5 times.

Electron number density profiles for simulated ammonia and simulated hydrazine have been obtained for 50 Ampere arcs at 2 psi, 6 psi, and 10 psi. A hydrogen/nitrogen mixture version of the CAPS code is being developed to provide comparisons with the experimental mixture data.

ACKNOWLEDGMENTS

This work was supported by the Air Force Office of Scientific Research under contract #F49620-94-1-0331 and the National Science Foundation under NSF Grant # CTS-9512489.

REFERENCES

1. T. Megli, H. Krier, and R. Burton, "A Plasmadynamics Model for Nonequilibrium Processes in N₂/H₂ Arcjets," AIAA 95-1961, 26th AIAA Plasmadynamics and Lasers Conference, San Diego, CA, June 19-22, 1995.
2. D. Keefer, D. Burtner, T. Moeller, and R. Rhodes, "Multiplexed Laser Induced Fluorescence and Non-equilibrium Processes in Arcjets," AIAA 94-2656, 25th AIAA Plasmadynamic and Lasers Conference, Colorado Springs, CO, June, 1994.

3. S. Miller, and M. Martinez-Sanchez, "Nonequilibrium Numerical Simulation of Radiation Cooled Arcjets," IEPC-93-218, *Proceedings of the 23rd International Electric Propulsion Conference*, Vol. 3: 2032-2050, Published at The Ohio State University, Columbus OH, 1993.
4. G. W. Butler, B. A. Kashiwa, and D. Q. King, "Numerical Modeling of Arcjet Performance," AIAA 90-1474, AIAA 21st Fluid Dynamics, Plasma Dynamics and Lasers Conference, Seattle, WA, June, 1990.
5. W. L. Wiese, D. R. Paquette, and J. E. SolarSKI, "Profiles of Stark-Broadened Balmer Lines in a Hydrogen Plasma," *Phys. Rev.*, 129:1225-1232, February, 1963.
6. H. Griem, *Plasma Spectroscopy*, McGraw-Hill, 1964, pp. 129-167.
7. T. Moeller, D. Keefer, and R. Rhodes, "Cascade Arc Studies of Nonequilibrium Hydrogen Plasmas," AIAA 96-3294, 32nd AIAA/ASME/SAE/ASEE Joint Propulsion Conference, Lake Buena Vista, FL, July 1-3, 1996.
8. R. Gonzalez, and P. Wintz, *Digital Image Processing*, Addison-Wesley Publishing, Ontario, 1977, pp. 199-209.
9. T. Moeller, D. Keefer, and R. Rhodes, "Studies of Nonequilibrium Hydrogen/Nitrogen Plasmas using a Cascade Arc," AIP Conference Proceedings 387, p. 317, The Space Technology and Applications International Forum (STAIF-97), Albuquerque, NM, Jan. 1997.
10. H. U. Griem, *Spectral Line Broadening by Plasmas*, Academic Press, New York, 1974.
11. W.H. Press, S.A. Teukolsky, W.T. Vetterling, and B.P. Flannery, Numerical Recipes in FORTRAN, 2nd ed. Cambridge University Press, Cambridge, 1992.
12. D.H. Oza, R.L. Greene, and D.E. Kelleher, "Collisional Broadening of the Balmer- α Transition of H and He⁺ in Plasmas," Physical Review A, Vol. 37, No. 2, Jan. 1988.
13. T. Moeller, D. Keefer, and R. Rhodes, "Nonequilibrium Hydrogen/Nitrogen Plasmas Studies Using a Cascade Arc," IEPC 97-063, 25th International Electric Propulsion Conference, Cleveland, OH, August, 1997.
14. R. Rhodes, and D. Keefer, "Non-equilibrium Modeling of Hydrogen Arcjet Thrusters," IEPC-93-217, *Proceedings of The 23rd International Electric Propulsion Conference*, Vol. 3: 2020-2031, Published at The Ohio State University, Columbus, OH, 1993.
15. K. Y. Cho, "Non-Equilibrium Thermodynamic Models and Applications to Hydrogen Plasmas," Ph.D. Thesis, Georgia Institute of Technology, March 1988.
16. A. D. Gosman and W. M. Pun, "Calculation of Recirculation Flows," Report No. HTS/74/12, Dept. of Mechanical Engineering, Imperial College, London, 1974.

17. C. M. Rhie, "A Pressure Based Navier-Stokes Solver," AIAA paper 86-0207, 24th AIAA Aerospace Sciences Meeting, " Reno, Nevada, January 1986.
18. T. M. Moeller, "Comparison of Experimental and Numerical Results for Radiation Cooled and Water Cooled Hydrogen Arcjets," *Proceedings of the 23rd International Electric Propulsion Conference*, Vol. 3: 1979-1988, Published at The Ohio State University, Columbus OH, 1993.
19. T.M. Moeller, "Comparison of Experimental and Numerical Results for Radiation Cooled and Water Cooled Hydrogen Arcjets," Masters Thesis, University of Tennessee Space Institute, 1993.
20. R. P. Rhodes, and D. Keefer, "Numerical Modeling of a Radio Frequency Plasma in Argon," *AIAA Journal*, Vol. 27, No. 12, December 1989, pp. 1779-1784.
21. R. Rhodes and D. Keefer, "Comparison of Model Calculations with Experimental Data from Hydrogen Arcjets," Paper 91-111, 22nd International Electric Propulsion Conference, Viareggio, Italy, October, 1991.
22. D. Keefer, D. Burtner, T. Moeller, and R. Rhodes, "Multiplexed Laser Induced Fluorescence and Non-equilibrium Processes in Arcjets," AIAA 94-2656, 25th AIAA Plasmadynamic and Lasers Conference, Colorado Springs, CO, June, 1994.
23. C. Park, Non-equilibrium Hypersonic Aerothermodynamics, John Wiley & Sons, New York, 1990.
24. R. R. Mikatarian, C.J. Kau, and H.S. Pergament, "A Fast Computer Program for Nonequilibrium Rocket Plume Predictions," AeroChem TP-282, August 1972.
25. K. K. Kuo, Principles of Combustion, John Wiley & Sons, New York, 1986.
26. R. S. DeVoto, "The Transport Properties of a Partially Ionized Monatomic Gas," Ph.D. Thesis, Stanford University, 1965.
27. S. Chapman and T.G. Cowling, Mathematical Theory of Non Uniform Gases, 3rd ed., Cambridge University Press, New York, 1970.
28. J.O. Hirschfelder, C.F. Curtiss, and R.B. Bird, Molecular Theory of Gases and Liquids, John Wiley & Sons, 1964.
29. R. Siegal, and J.R. Howell, Thermal Radiation Heat Transfer, 3rd ed., Hemisphere Publishing Corp., Washington, D.C., 1992.

30. L. M. Smith, D. Keefer, and S.I. Sudharsanan, "Abel Inversion Using Transform Techniques," *J. Quant. Spectrosc. Radiat. Transfer*, 39:367-373, 1988.
31. Janev, et al, Elementary Processes in Hydrogen Helium Plasmas, Springer-Verlag, New York, 1987.

Table 1. Reaction Rates for Hydrogen.

	Reaction	a	n	E
1	$H + H + M \leftrightarrow H_2 + M$	6.40e+17	1.0	0.
2	$H^+ + e + M \leftrightarrow H + M$	5.26e+26	2.5	0.
3	U of I			
U of I	$H_2 + e \rightarrow H + H + e$	1.87e-3	-3.73	0.
3	$H_2 + e \rightarrow H + H + e$	1.91e+11	-1.0	-203.
4	$H^+ + e \rightarrow H + h\nu$	3.77e+13	0.58	0.
	fast rates			
5	$H^+ + e + e \leftrightarrow H + e$	7.08e+39	4.5	0.
	slow rates			
5r	$H^+ + e + e \rightarrow H + e$	2.19e+41	5.06	0.
5i	$H + e \rightarrow H^+ + e + e$	1.81e+14	0.	-244750

Table 2. Comparison of Experimentally Determined Electric Field (V/cm) with UTSI Cascade Arc Plasma Simulation (CAPS) Code Values.

	Equilibrium Simulation	"Slow" Non-Equilibrium	"Fast" Non-Equilibrium	"U of I" Non-Equilibrium	Experiment
Case 1: 2.0 psi	46.4	95.7	42.0	33.4	36.0 ± 1.2
Case 2: 6.0 psi	46.3	64.9	43.9	44.1	44.2 ± 1.2

Table 3. Experimentally Determined Electric Field (V/cm) for Hydrogen and Hydrogen/Nitrogen Mixtures.

	Hydrogen	Simulated Ammonia	Simulated Hydrazine
Case 1: 2.0 psi	36.0 ± 1.2	26.4 ± 0.7	26.2 ± 0.8
Case 2: 6.0 psi	44.2 ± 1.2	38.8 ± 1.1	35.1 ± 0.9

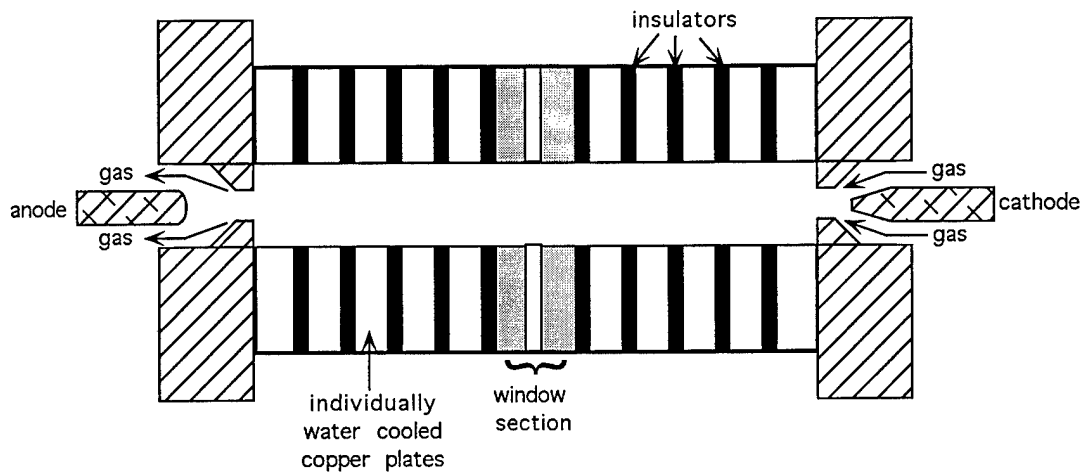


Figure 1. Cascade Arc Assembly.

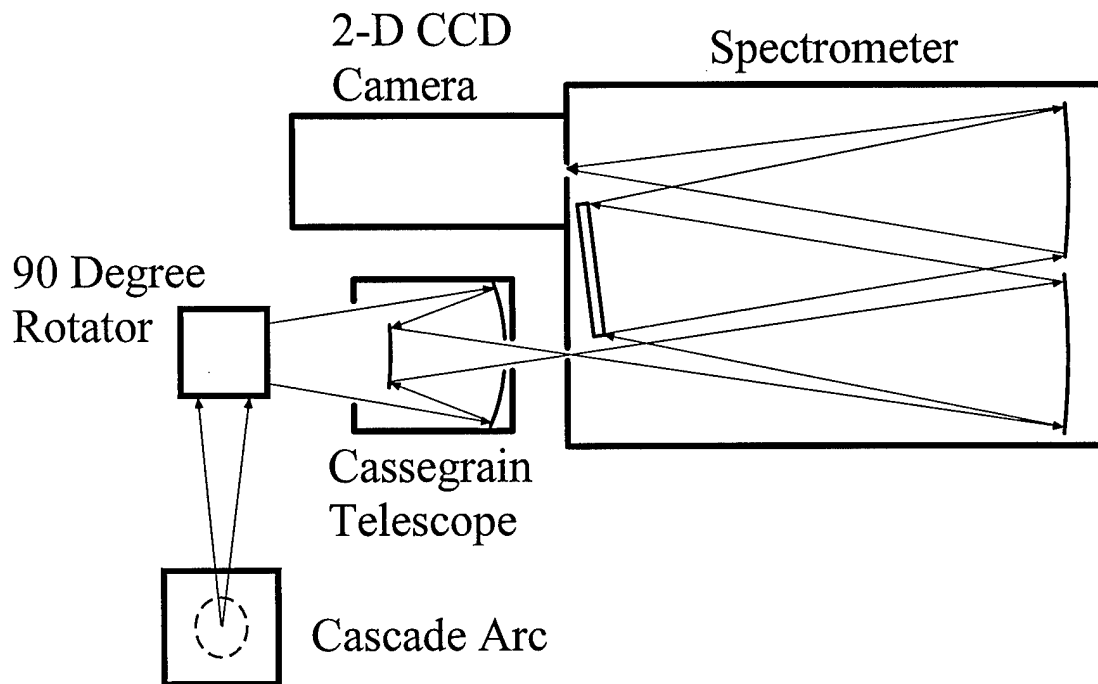


Figure 2. Schematic of the optical setup.

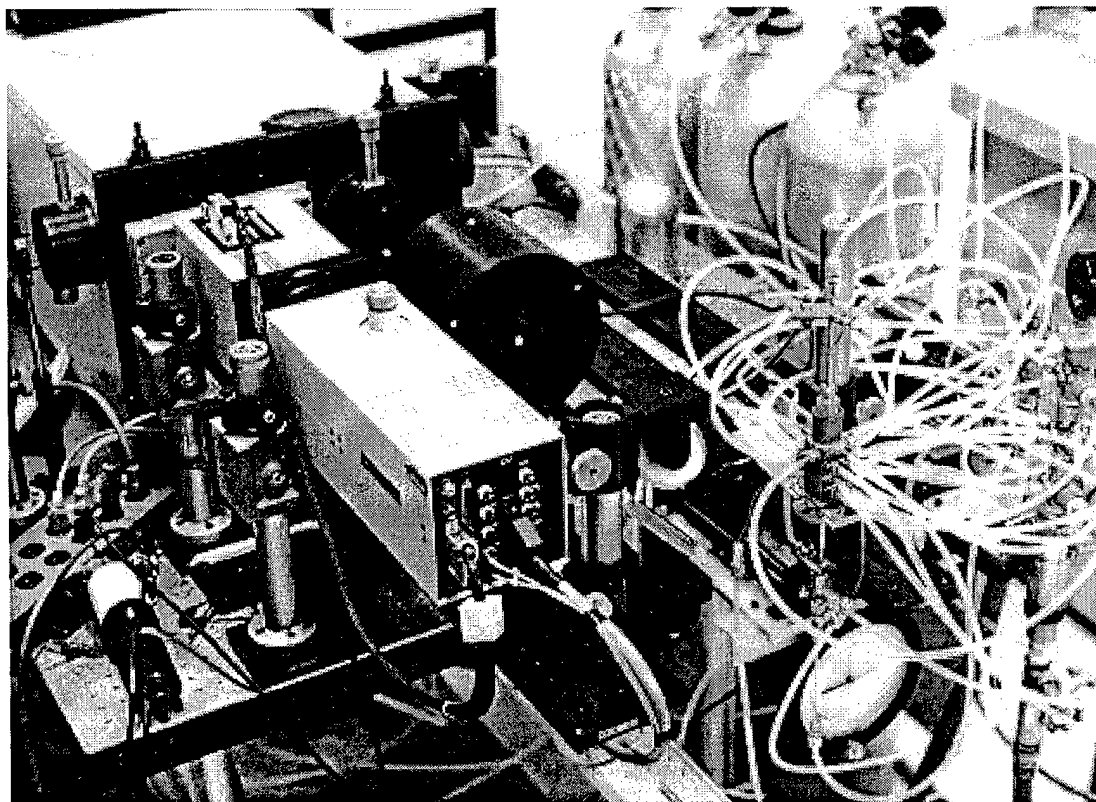


Figure 3. Picture of the UTSI Cascade Arc Facility and external optics.

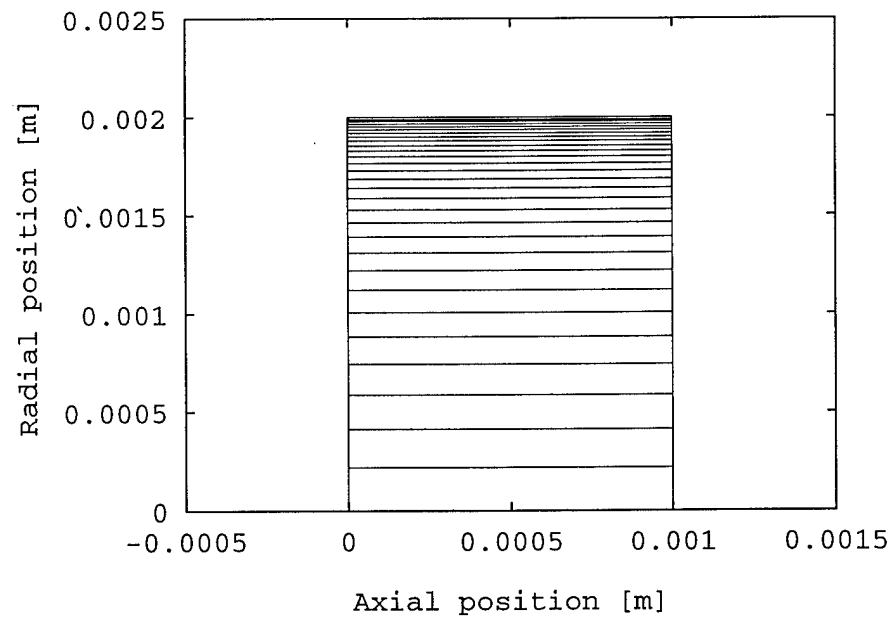


Figure 4 Computation grid (in spatial coordinates) used in the CAPS code simulations.

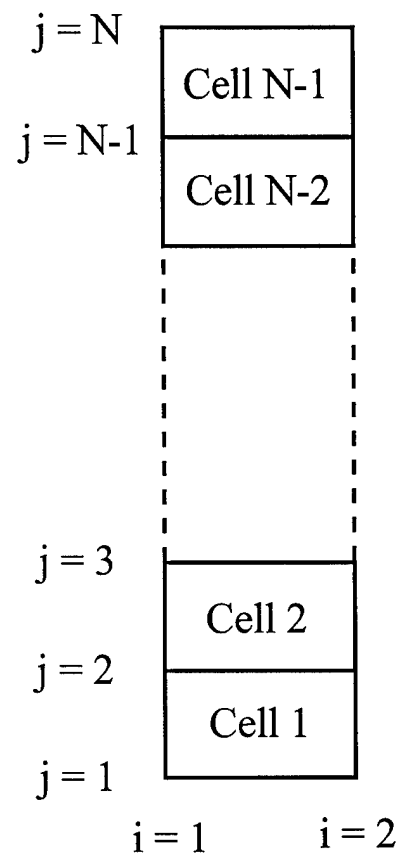


Figure 5 Computation cells surrounding points in a transformed computation grid. There are N grid points and $N-1$ cells in the radial direction.

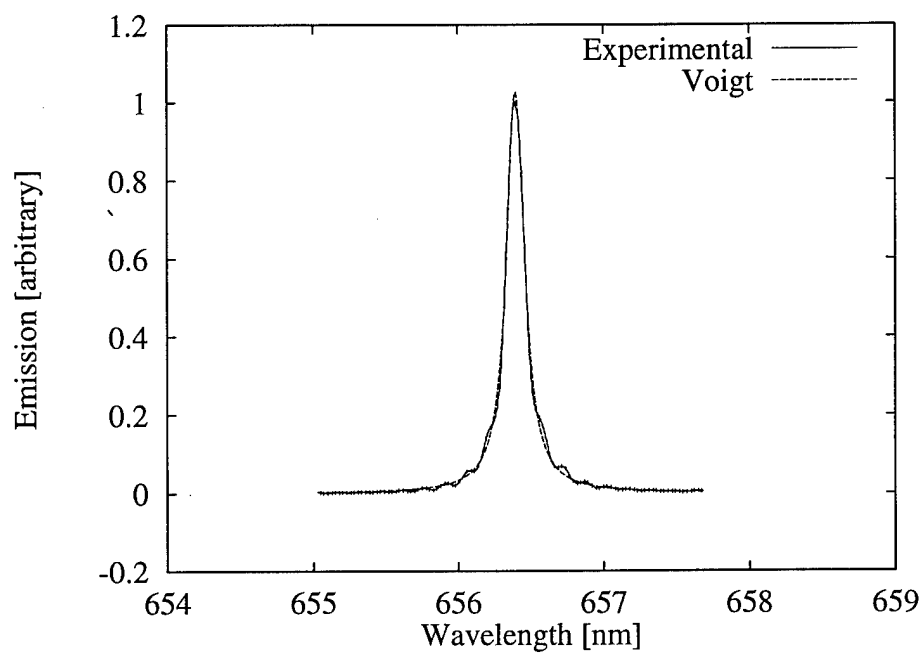


Figure 6. Measured and Fitted Theoretical Voigt Lineshapes of H_{α} Line in a 50 Amp Hydrogen Arc at 6.0 psi at a Radius of 1.5 mm.

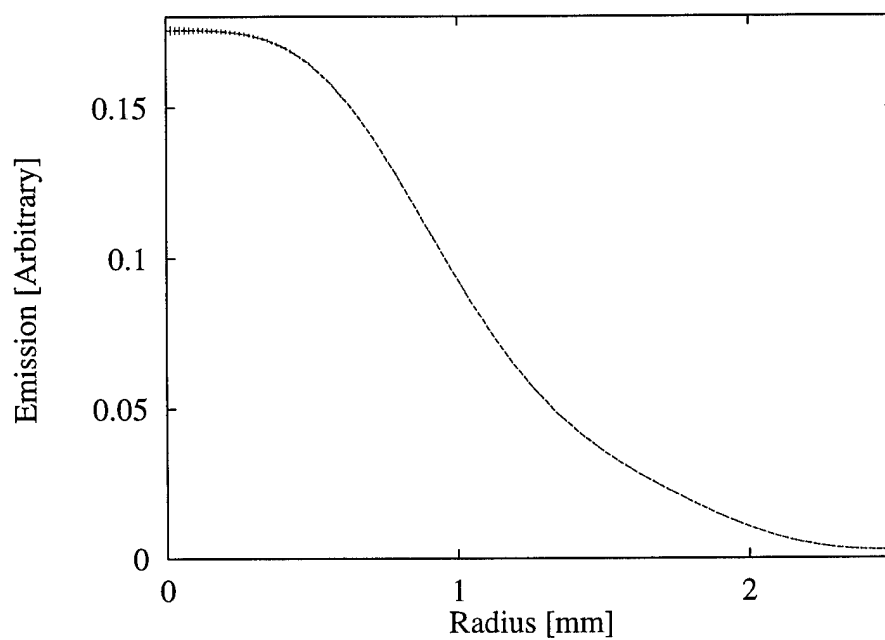


Figure 7. Radial profile of integrated emission for a 50 Amp hydrogen arc at 6 psi.

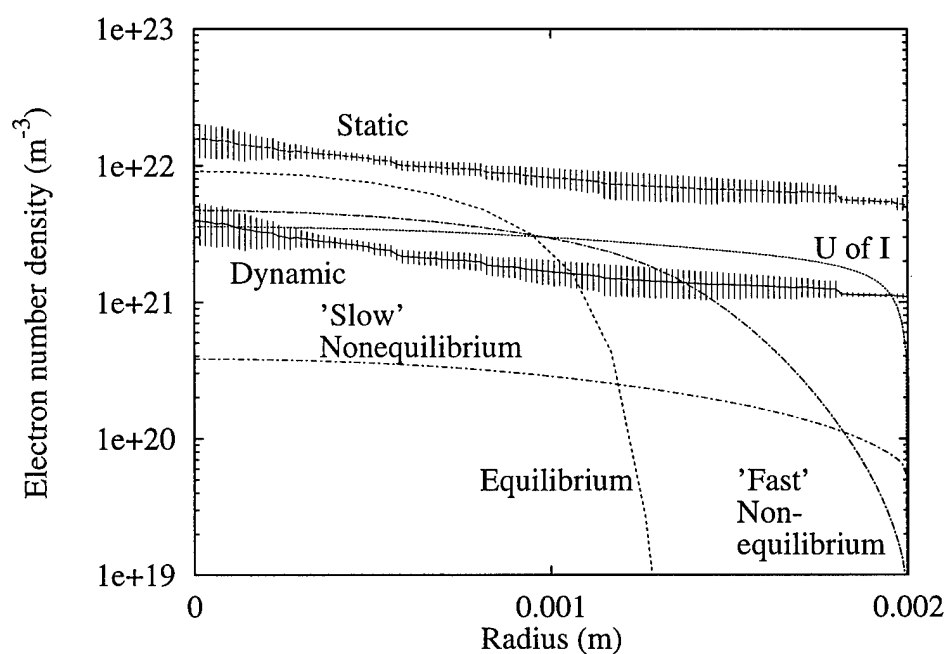


Figure 8. Comparison of Experimental and Numerical Radial Distributions of Electron Number Density in a 50 Amp Hydrogen Arc at 2.0 psi. "Fast" and "slow" represent nonequilibrium computer simulations using two different chemical kinetic rates for the ionization of hydrogen due to electrons. "U of I" indicates a finite rate solution using a different rate for the dissociation of hydrogen by electrons.

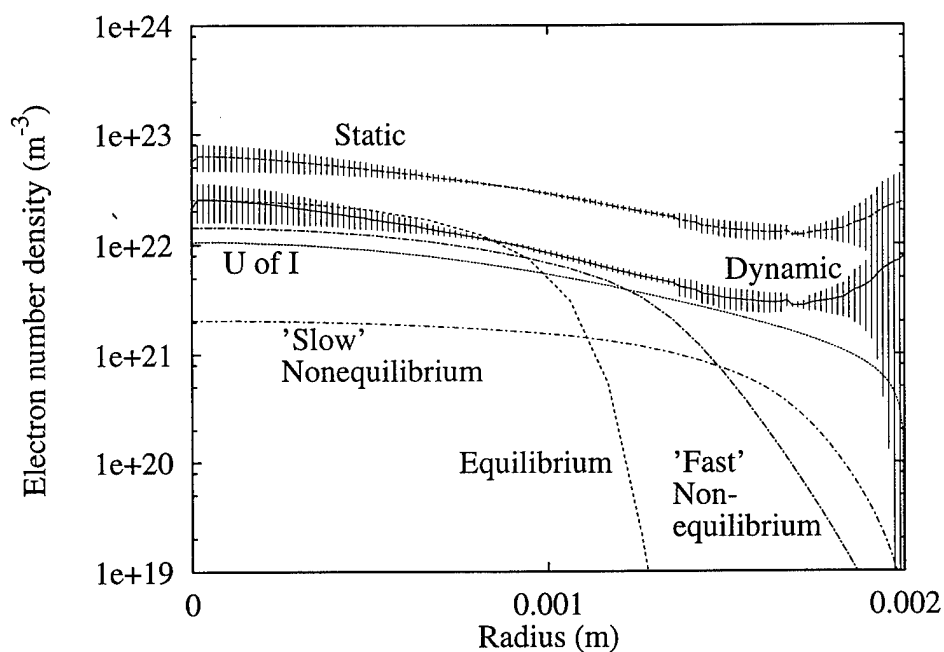


Figure 9. Comparison of Experimental and Numerical Radial Distributions of Electron Number Density in a 50 Amp Hydrogen Arc at 6.0 psi. "Fast" and "slow" represent nonequilibrium computer simulations using two different chemical kinetic rates for the ionization of hydrogen due to electrons. "U of I" indicates a finite rate solution using a different rate for the dissociation of hydrogen by electrons.

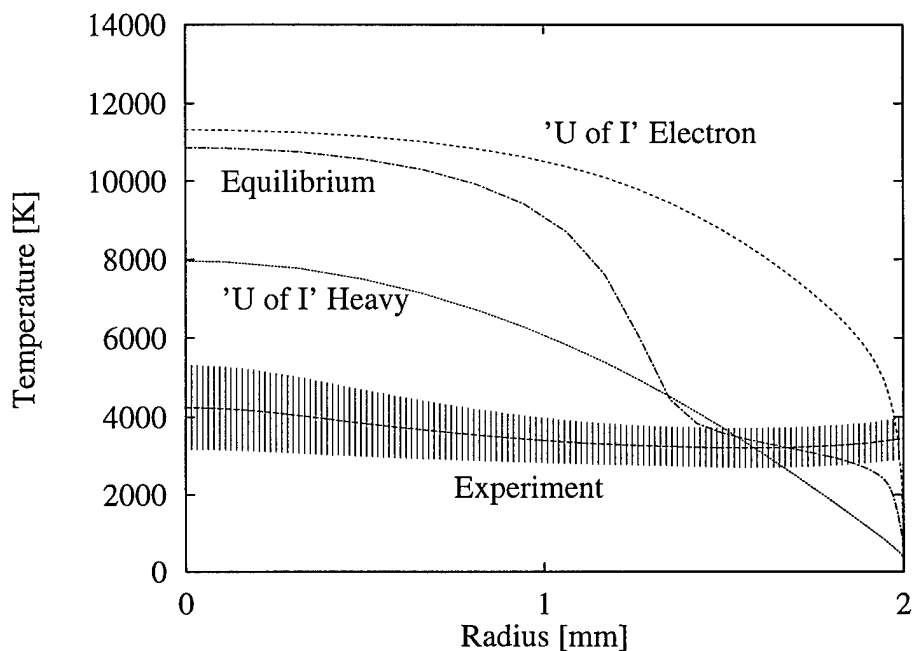


Figure 10. Comparison of Experimental and Numerical Radial Distributions of the Plasma Temperature in a 50 Amp Hydrogen Arc at 2.0 psi. "U of I" indicates a finite rate solution using "U of I" kinetics.

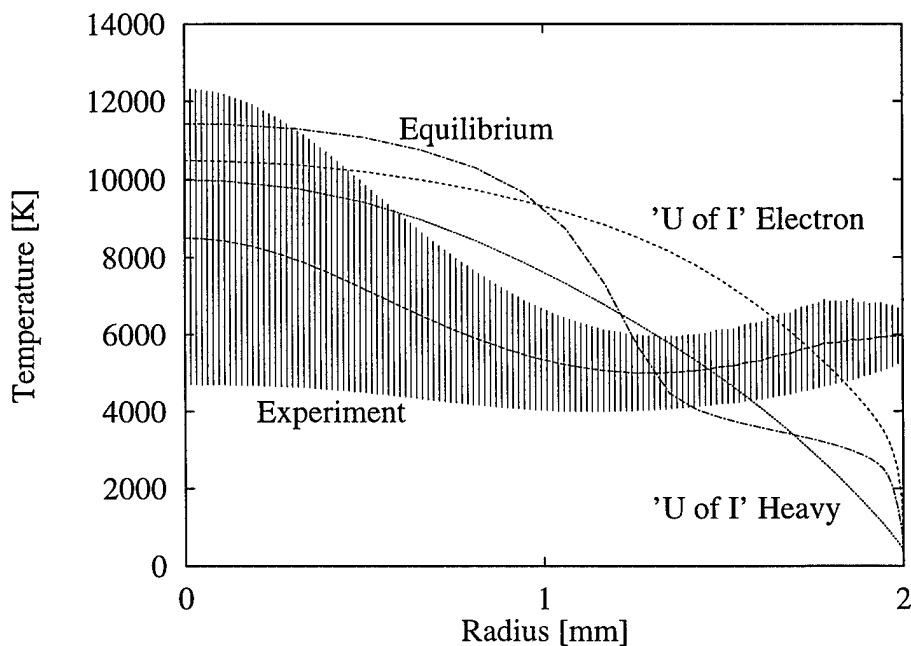


Figure 11. Comparison of Experimental and Numerical Radial Distributions of the Plasma Temperature in a 50 Amp Hydrogen Arc at 6.0 psi. "U of I" indicates a finite rate solution using "U of I" kinetics.

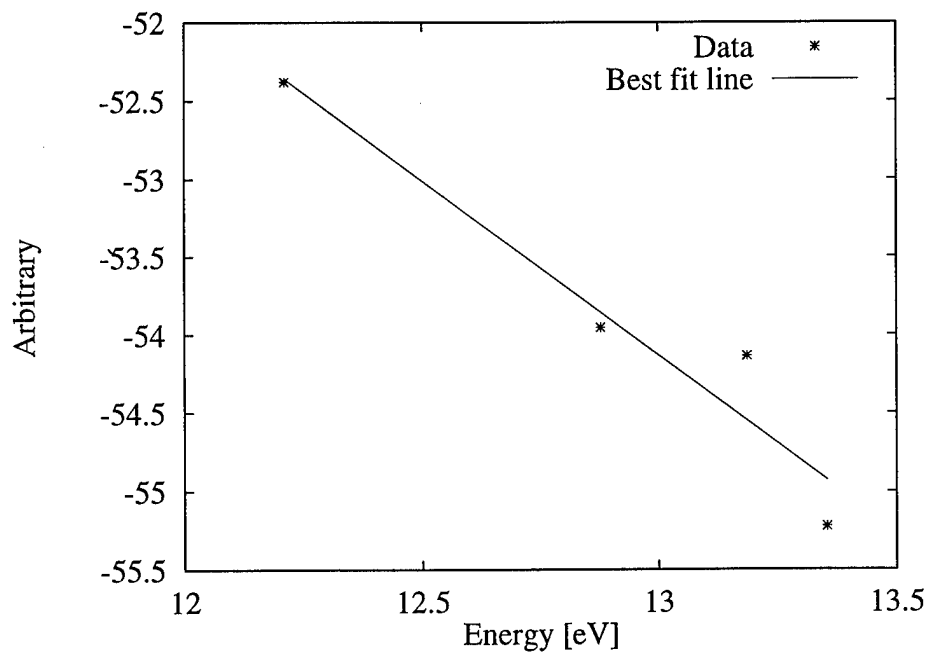


Figure 12. Boltzmann Plot Using the H_{α} , H_{β} , H_{γ} , and H_{δ} Lines in a 50 Amp Hydrogen Arc at 6.0 psi at a Radius of 1.5 mm.

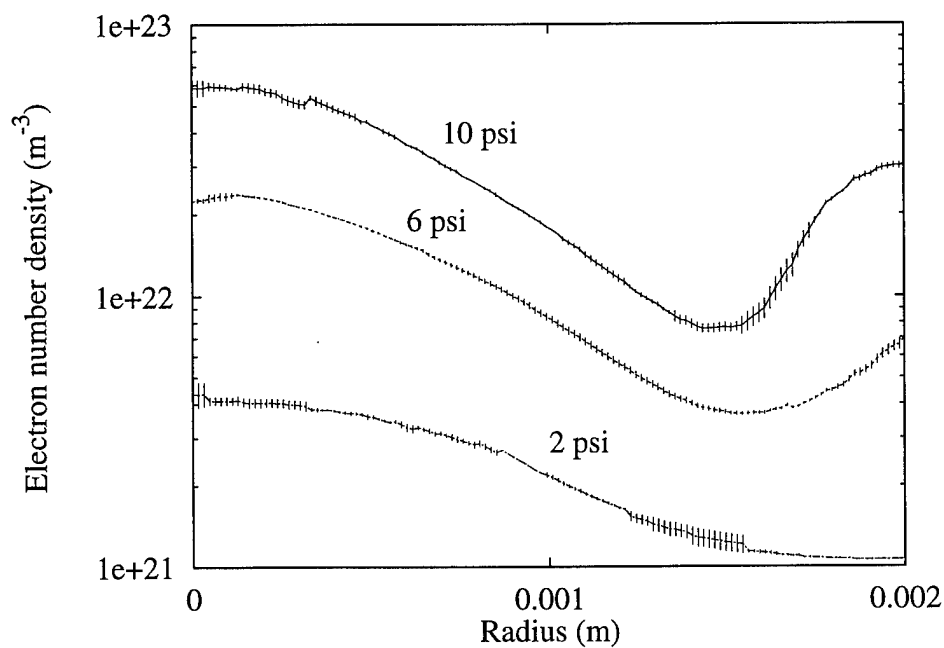


Figure 13. Radial Distributions of Electron Number Densities for Simulated Ammonia (NH_3) at 2.0 psi, 6.0 psi, and 10.0 psi.

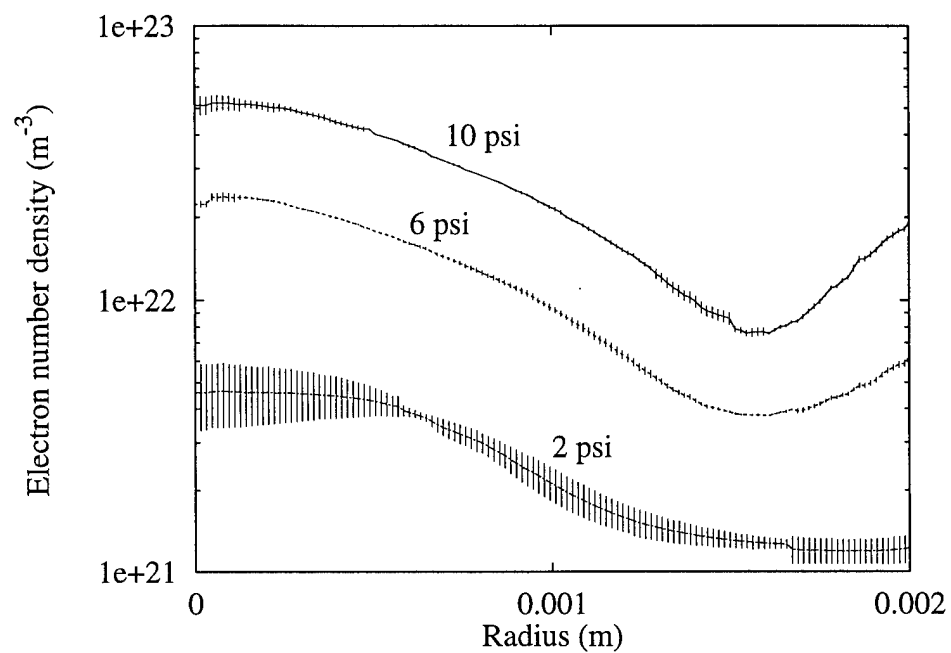


Figure 14. Radial Distributions of Electron Number Densities for Simulated Hydrazine (N_2H_4) at 2.0 psi, 6.0 psi, and 10.0 psi.



AIAA 96-3294

**Cascade Arc Studies of Nonequilibrium
Hydrogen Plasmas**

Trevor Moeller, Dennis Keefer and Robert Rhodes
University of Tennessee Space Institute
Tullahoma, TN 37388

**32nd AIAA/ASME/SAE/ASEE
Joint Propulsion Conference
July 1-3, 1996 / Lake Buena Vista, FL**

CASCADE ARC STUDIES OF NONEQUILIBRIUM HYDROGEN PLASMAS

Trevor Moeller*, Dennis Keefer†, and Robert Rhodes‡

University of Tennessee Space Institute
B. H. Goethert Parkway
Tullahoma, TN 37388

Abstract

A cascade arc facility has been constructed at UTSI to study the effect of nonequilibrium transport properties in hydrogen-nitrogen arcjet propellant plasmas. These studies will be used to guide development of the physical models required for further development of arcjet computational codes. The cascade arc has been operated on hydrogen at 50 Amps and at pressures of 2.0 psi and 6.0 psi. Preliminary spatially resolved spectral data at these conditions have been collected for the Balmer H_{α} line. Theoretical, Stark broadened, H_{α} lineshapes have been fitted to the experimental lineshapes to determine the radial distributions of electron number density. These number densities were compared to values taken from the nonequilibrium and equilibrium cascade arc simulations. The simulations underpredict the peak experimental number densities; however, the profile of the nonequilibrium solution matches the experiment.

Introduction

Arcjets offer significant advantages for satellite station keeping and maneuvering, since their specific impulse can be more than twice that of conventional resistojets or chemical thrusters commonly used for these missions. Four commercial satellites using these new arcjet thrusters for orbit maintenance are already in use [1]. Current arcjet thruster performance, however, is far below the limits of an ideal arcjet, leaving room for significant improvements. Future improvements in arcjet performance require that a larger fraction of the propellant passing through the constrictor be heated to high temperatures. Computational codes can be used to guide refinements in the basic arcjet configuration which would lead to more uniform radial temperature profiles, and a number of arcjet codes have been

developed for this purpose [2,3,4,5]. However, it is now clear that there are important nonequilibrium processes in the propellant plasma which must be understood before adequate physical models can be constructed for use in these computational codes. A cascade arc facility has been constructed at UTSI which permits measurements of nonequilibrium transport properties to be made on a controlled nonequilibrium propellant plasma to guide development of the physical models required for further development of the computational codes.

A computational code has been under development at UTSI since 1986 to aid in interpretation of experiments and to develop a better understanding of the physical processes in laser thermal propulsion and arcjet thrusters [6]. The code has evolved to

* Graduate Research Assistant, Student Member, AIAA

† B.H. Goethert Professor of ES, Senior Member, AIAA

‡ Senior Engineer, Senior Member, AIAA

include nonequilibrium processes, and by comparison with arcjet experimental results has highlighted the importance of nonequilibrium processes in the operation of arcjet thrusters. Some nonequilibrium effects shown to be of particular importance are species diffusion, thermal conductivity and electrical conductivity. Species diffusion and thermal conductivity, including radiation transfer, determine the rate of energy transport from the hot arc core into the cooler surrounding propellant flow. Electrical conductivity is particularly important in the cool, highly nonequilibrium plasma boundary layer near the anode surface. The electrical conductivity controls the voltage drop in the anode region which has a large effect on the heat transfer to the anode wall and on the overall electrical efficiency of the arcjet.

Reasons For Utilizing a Cascade Arc Rather Than an Arcjet

Some of the most important chemical and transport processes in an arcjet arc, e.g. radial species diffusion and recombination, occur on time scales that are comparable to the convective times in an arcjet. This fast convection produces the strong axial gradients found in an arcjet plasma. Therefore, the plasma conditions at a given point in an arcjet depend strongly on the previous history of the plasma passing through that point. Comparison of code predictions with measurements in this case requires that the entire upstream flow field be accurately predicted. Differences between measured and predicted quantities could be due to inaccuracies in the models at any point upstream of the measurement location. This makes it very difficult to assess which model mechanisms or rates should be altered to improve the code.

Cascade arcs have long been used as a means to measure the fundamental atomic constants and transport properties of high temperature gases [7]. The cascade arc has

a diameter similar to that of an arcjet constrictor but the flow velocity is much smaller and the length of the arc is tens of diameters as compared to one diameter in an arcjet. This produces an arc with similar properties to an arcjet but with negligible axial gradients. The radial temperature profiles in the cascade arc are controlled primarily by diffusive transport properties rather than convection. In the cascade arc, where there are no significant axial gradients, the nonequilibrium plasma parameters are determined by a balance between radial diffusion and chemical reactions and an axially constant but radially dependent energy input. The plasma properties depend on the local conditions at the measurement station rather than a complex convolution of all the conditions upstream of the point of measurement. Differences observed between code predictions and measured quantities are more easily related to specific reactions or diffusion rates which must be modified to improve the code models.

The arc in an arcjet is confined within a constrictor/nozzle/anode made of tungsten. Accurate radial spatial resolution of the optical measurements is required for comparison with code predictions. Emission measurements require Abel inversion to obtain this spatial resolution, and accurate Abel inversion requires axial symmetry of the arc. It is difficult to obtain optical access through the typical large diameter tungsten piece which forms the arcjet constrictor/nozzle/anode. Some optical observations of an arcjet arc have been made through holes drilled into the tungsten constrictor region [8,9]. However, this creates an opening at one azimuthal location and axial symmetry of the arc becomes compromised. It is also difficult to provide the optical access required for accurate absolute optical calibration. In the cascade arc the optical access can be made symmetric, preserving symmetry of the arc, and adequate solid angles are available to provide good absolute calibrations.

Accurate optical measurements of the radial profiles, together with analysis based on an appropriate one-dimensional computational code, will permit validation of the chemical kinetics and diffusive transport models and provide a basis for the development of physical models needed for the arcjet codes being developed.

UTSI Equilibrium/Nonequilibrium Cascade Arc Computer Code

The equilibrium and nonequilibrium UTSI arcjet computer codes have been modified into one-dimensional nonequilibrium and equilibrium cascade arc computer codes [10]. At present these codes model a H_2 , H , H^+ , e hydrogen system. Both codes include species diffusion and radiation transport. The nonequilibrium version has a two-temperature model for heavy species and electrons and a finite rate chemistry kinetics model. In both codes it is assumed that the pressure is constant, the radial velocity is zero, and the radial current density is zero. The required mass flow is assured by adjustment of velocity levels. The consequence of these assumptions is that species production and diffusion are locally balanced and total production is balanced by wall losses for the axial momentum, energy, electron energy, and species.

The transport properties for both the equilibrium and nonequilibrium versions of the UTSI cascade arc computer code are calculated using a computer code written by Cho based on the procedures developed by DeVoto [10]. These models start with experimental or calculated energy dependent collision cross-sections, calculate the collision integrals based on one of several interaction models and use combinations of the collision integrals to determine the transport properties. Electrical conductivity and electron thermal conductivity depend on collisions between electrons and heavy species in the mixture, while viscosity and heavy gas thermal

conductivity depend primarily on collisions between the heavy species.

The Cho model makes the following assumptions when used with a two-temperature nonequilibrium plasma model. The fundamental cross-section data describes the interaction of one atom or molecule with another, and depends only upon collision energy and the identity of the colliding pair. The nonequilibrium plasma is described by a two-temperature model where a Maxwellian distribution at a unique electron temperature describes the kinetic energy of the electrons. The electron temperature is used to determine the collision energy for all collisions involving electrons, since the relative velocity of a collision involving an electron is close to the velocity of the electron. The heavy gas temperature is used to determine the collision energy for all other collisions.

Species nonequilibrium is treated by solving species conservation equations with production terms containing the kinetic reaction rates for the ionization, dissociation, and recombination processes included in the plasma model. In addition, a significant amount of the energy transport between the electrons and the heavy species results when an electron acts as the third body in a reactive collision. Therefore, the recombination reaction rates can influence the electron to heavy gas temperature ratio, as well as the gas composition. The reaction rates for the hydrogen system used in the computer simulations presented in this paper are shown in Table 1. These rate coefficients were adapted from those given by McCay and Dexter [12] with the recombination rate slightly modified to fit the data from Park [13].

UTSI Cascade Arc Facility

The UTSI cascade arc is comprised of individually water cooled copper plates separated by electrical insulators (Figure 1).

These plates are 1/8 " thick and form a 4 mm diameter arc channel that is approximately 40 mm long. The insulators are ceramic paper or mica 0.010" thick. A modified plate with windows allows optical access. This section is located in the center of the cascade arc to minimize end effects. The cathode is a 0.250" diameter thoriated tungsten rod with a 60 degree cone on the end. The anode is 0.360" diameter thoriated tungsten rod with a blunt end. Both electrodes are cooled by a water jet impinging on their back surface. The arc is driven by a 50 Amp, 600 V power supply. A cascaded centrifugal pump delivers 11 gal/min of water at 200 psi to cool the copper plates and electrodes. The cascade arc is positioned vertically to eliminate arc asymmetries caused by buoyancy.

Accurate measurement of plasma parameters requires careful integration of the optical design with the design of the central window section. Abel inversion of the emission data is needed to provide radial measurements of the plasma properties [14]. Absolute emission measurements are necessary to determine species concentrations and provide a more accurate measurement of plasma temperatures. Absolute calibration will be performed using traceable calibration lamps. Since the lamp cannot be placed within the cascade structure, this requires that the limiting aperture is not at the cascade disk or external optics, but is determined by the internal optics of the spectrometer. To provide a small entrance solid angle for the cascade window section and to avoid off-axis aberrations, an adjustable, reflective cassegrain optical collection system is used. This collects light from the arc and directs it into a 1.25 meter focal length spectrometer so that the primary mirror in the spectrometer is overfilled (Figure 2). Before entering the cassegrain telescope the light from the arc is rotated ninety degrees so that the radial dimension of the arc image lies along the slit. A two-dimensional optical multichannel analyzer (OMA) with

image intensifier is used to collect and digitize the data. This detector has a 512 x 512 pixel detector array with 19 μm pixel spacing and is used to simultaneously acquire spectral data at many radial locations. The magnification of the optical system is approximately 1.0 giving 200 pixels across the 4 mm diameter arc channel.

Data Analysis and Preliminary Experimental Results

The cascade arc facility has been utilized to generate 50 Amp hydrogen arcs at 2.0 psi and 6.0 psi. Preliminary spectral data of the 656.28 nm Balmer alpha, H_{α} , line were collected and are currently being analyzed. At the pressure range of interest, the H_{α} is broadened significantly by the Stark effect [14]. Because the Stark effect has strong dependence on electron number densities and depends only slightly on temperature, the electron number density of a plasma can be determined independently of the plasma temperature by fitting theoretical profiles to the experimentally measured H_{α} lines [15]. The 2-D OMA captures spectral intensity data at many spatial locations across the arc simultaneously. Because this intensity data is a line-of-sight projection of the emission data onto a one-dimensional axis, it must be Abel inverted to obtain a radial profile of the spectral emission. Theoretical profiles can then be fitted to this radial distribution of spectral lines to determine the radial variation of electron number density.

The Abel inversion is performed using a modern approach that utilizes integral transforms [16]. In this method, the Abel inversion of line-of-sight intensity data into radially distributed emission data is accomplished by taking the Fourier transform of the intensity data and then performing an inverse Hankel transform. Incorporated in this inversion technique is a method for determining the center of the

data that minimizes asymmetries. Because Abel inversion implies radial symmetry, any asymmetry is assumed to be noise. Since the Fourier transform of symmetric data is real and the Fourier transform of asymmetric data has imaginary components, the imaginary components of asymmetric data is noise by definition. Therefore, by shifting the data so that the imaginary component of the transform is a minimum, the center can be found. Because fast Fourier transforms (FFT's) can be implemented in the method described above, this Abel inversion process can be performed much faster than conventional methods.

The following algorithm has been used to implement this Abel inversion approach in our data analysis. (1) A fast Fourier transform (FFT) is performed on the intensity data. (2) High frequency noise is filtered out of spectral data using an optimal, finite impulse response (FIR), low band pass filter. (3) The inverse fast Fourier transform (IFFT) is performed on the data. These first three steps smooth the spectral data by filtering out high frequency noise. The Abel inversion is performed next. (4) Perform FFT on spatial data. (5) Filter spatial high frequency noise using another FIR, low band pass filter. (6) Center transformed data by shifting to minimize imaginary component of transformed data. (7) Throw away imaginary part of shifted, transformed data. This step eliminates noise (asymmetries) in the data. (8) Perform the inverse Hankel transform to obtain the Abel inverted data.

Seventh order H_{α} spectral data were collected using a 316 groove/mm echelle diffraction grating. A Schott OG550 filter which passes wavelengths above 600 nm was used to eliminate corruption of the seventh order H_{α} line with higher order beta, gamma, and delta lines. The OMA detector exposure times were 8.0 seconds for the 6.0 psi case and 14.0 seconds for the 2.0 psi case. The 2.0 psi case requires

longer exposure times because the intensity of the radiation is lower for this smaller pressure. The gain of the OMA intensifier was 10 for both cases.

Figure 3 shows the contour plot of the intensity data for the 6.0 psi case. The data varies spectrally along the abscissa and spatially along the ordinate. The arc image has 512 spectral pixels and 256 spatial pixels. Wavelength calibration was performed on the spectral pixels using seven lines from a low density neon calibration source. The spatial pixels were calibrated by taking images of a 50 μm vertical slit backlit by a continuous source and placed in the same position as the arc when the cascade is in operation. By moving the vertical slit across the location of the arc with a translation table, the spatial pixels were associated with a radial position across the arc region.

Abel inversion was performed using the method described above. The spectral FIR smoothing filter had a cutoff frequency of 14 percent of the Nyquist frequency while the spatial filter had a cut off frequency of 5 percent of Nyquist frequency. The radial profile of the spectral row containing the peak emission for the 6.0 psi case is shown in Figure 4. The error bars on the emission of plus or minus one standard deviation of the output noise are estimates of the error associated with the Abel inversion. This error was calculated from the variance of the input noise and the spatial bandpass cutoff frequency using a method developed by Smith [17]. Smith shows that "the variance of the output noise is directly proportional to the variance of the input noise and to the bandwidth [of the filter], and inversely proportional to the radial distance from the origin" [17]. As can be seen in Figure 4, the error is inversely proportional to the radius. The error asymptotically approaches infinity as the radius goes to zero. However, when the radius is as little as 20 μm , the standard

deviation of the emission has decreased to three percent of the emission and continues to decrease with radius. The emission has not decreased to zero at 2 mm, which is the radius of the arc constrictor. There are two explanations for this feature. First, the plasma might be slightly bowed into the optical channels leading to the windows. Second, reflections of light from the walls of the optical channel might be giving the appearance of a larger radius arc. The effects of the slit have not yet been deconvolved from the data presented here; however, initial deconvolution results indicate that the effects of the slit do not significantly alter the radial emission profile.

Theoretical Stark broadened H_{α} line profiles have been fitted to the radial distribution of the H_{α} spectral emission data shown in Figure 4 to determine a radial distribution of number densities. The fitting routine estimates an emission baseline value and then determines the best theoretical profile by minimizing the sum of the residual errors between the theoretical lineshape and the experiment lineshape over a range of electron number densities. The theoretical and experimental lineshapes are compared in Figures 5 and 6 showing the error bars previously discussed. The profile at a radius of 0.04 mm appears in Figure 5 for the 6.0 psi case; and the profile at 1.5 mm is shown in Figure 6. The theoretical profile fits the data better at the larger radius. This can be explained by the fact that the uncertainty of the Abel inverted data increases as the centerline is approached. At a radius of 0.04 mm the wings of the H_{α} line are smaller than predicted by theory, and the line is fitted well at a radius of 1.5 mm. For radii close to 2 mm, the signal to noise ratio is quite low and results in both poor fits that are much wider than theory and the overprediction of electron number densities. As mentioned earlier, the effects of the slit function have not yet been removed. Deconvolution of the slit function from the

data will make the experimental lineshapes slightly thinner resulting in a small increase in the deviation from theory. Experimental radial number density profiles are shown in the next section where they are compared with results from the UTSI cascade arc computer code.

Comparison of Numerical and Experimental Results

Comparisons of the radial distribution of calculated and experimental electron number densities for the 2.0 psi and 6.0 psi cases appear in Figures 7 and 8, respectively. At both pressures, the nonequilibrium and equilibrium simulations underpredict the experimentally determined electron number densities for all radii. The peak equilibrium number density is a factor of two smaller than the corresponding experimental value while the nonequilibrium value is two orders of magnitude smaller for the 2.0 psi case (Figure 7). Even though the equilibrium simulation predicts the peak electron number density better than the nonequilibrium simulation, the nonequilibrium distribution has nearly the same profile as the experimental data. Similar trends are seen at 6.0 psi (Figure 8). The peak equilibrium electron number density is five times smaller than the experimental value while the nonequilibrium value is almost 2 orders of magnitude smaller. However, like in the 2.0 psi case, the nonequilibrium simulation does a better job predicting the shape of the experimental profile. An interesting feature of the experimental number density profiles is the positive slope of the curve close to the wall of the arc channel at 2 mm. This feature is the result of relatively poor theoretical lineshape fits to the data in these regions. The signal to noise ratio has dropped to less than three at a radius of 1.8 mm for the 2.0 psi case and a radius of 1.65 mm for the 6.0 psi case. This low signal to

noise ratio results in unreliable electron number densities in these regions.

Table 2 is a comparison of the experimental electric field and power with the equilibrium and nonequilibrium code values. The experimental electric fields were determined by finding the slope of the best fit line through the potentials of the cascade plates. The experimental electrical power deposited into the plasma is calculated using:

$$\text{Power in} = I * E \quad (1)$$

where

I = Arc current

= 50.2 ± 0.1 Amps

E = Electric field

The experimentally determined power removed from an arc per unit length is calculated from the change in cooling water temperature and the mass flow rate through one of the water cooling channels in the window section (equation 2).

$$\text{Power out} = V * \rho * C_p * \Delta T / L \quad (2)$$

where

V = volumetric flow rate

= 0.8 ± 0.1 gal/min

ρ = density of cooling water

= 997 kg/m^3

C_p = specific heat of cooling water

= 4.18 kJ/kg-K

ΔT = rise in cooling water temperature

= $4.0 \pm 0.5 \text{ K}$ for both cases.

L = Length of window

section cooled by water channel.

= $0.42 \pm 0.01 \text{ cm}$.

The power removed from the plasma is the same for both cases because the rise in the cooling water temperature, determined using thermocouples, was the same at each pressure (the thermocouples are not accurate

enough to measure fractions of a degree; and therefore can only measure changes in temperature greater than one degree). As can be seen in Table 2, the measured power in and power out are the same within experimental uncertainty.

The electric fields from the equilibrium simulations overpredict the experimentally determined values by 50 percent for the 2.0 psi case and 15 percent for 6.0 psi case. These overpredictions increase to 220 percent and 75 percent for the nonequilibrium simulations at 2.0 psi and 6.0 psi, respectively. As a result of these overpredicted electric fields, the computer simulations predict higher power deposited into the flow than the experimental values. The electrical power deposited into the flow is calculated from the simulation results using equation (1). The power out for the computer simulations is the conduction of energy to the wall. The power deposited and removed from the plasma in the simulations are within 3.5 percent. Therefore, the computer simulations have converged and are conserving energy well enough that differences with experimental values can be attributed to the transport and chemical kinetic models used in the simulations.

Conclusions

The nonequilibrium cascade arc simulation predicts the experimentally determined electron number density profile even though the peak electron number densities from the equilibrium simulation more closely match the experiment. Neither the equilibrium nor the nonequilibrium computer simulation of the cascade arc correctly predicts the electric field and plasma power measured in the experiment. Assuming that the electric field is not a function of radius, the electrical power per unit length deposited into the flow can be written as

$$\begin{aligned}\frac{P_{in}}{\text{length}} &= I \cdot E = I \cdot \frac{J(r)}{\sigma(r)} \cdot A \\ &= \frac{I \cdot J(r) \cdot m_e \cdot v(r) \cdot A}{n(r) \cdot e}\end{aligned}\quad (3)$$

where

I = Current

E = Electric field = J/σ

A = Arc area.

$J(r)$ = Current density.

$\sigma(r)$ = electrical conductivity.

m_e = mass of electron.

e = electron charge.

$v(r)$ = collision frequency.

n_e = electron number density.

The parameters in this equation depend only on local conditions for a cascade arc, but would also depend on upstream conditions in an arcjet. The upstream independence of plasma conditions in the cascade arc allows simulation errors to be attributed exclusively to transport and kinetic model inadequacies and not to cumulative upstream errors due to large convection terms. The power deposited into the plasma is proportional to the collision frequency and inversely proportional to the electron number density (equation 3). This is consistent with the experimental and numerical results in this paper. At both 2.0 psi and 6.0 psi the computer simulations overpredict the power in the arc plasma and underpredict the electron number density. The nonequilibrium simulation has a larger discrepancy with the measured power than the equilibrium simulation; and therefore, the nonequilibrium simulation underpredicts the electron number density more than the equilibrium simulation (see Figures 7 and 8). The nonequilibrium simulation electron number densities are as much as two orders of magnitude too low, while the plasma power is over predicted by less than an order of magnitude. Therefore, the collision frequency, as well as the electron number

densities, used in the simulations must be in error (see equation 3). This indicates that the transport property and finite rate chemical kinetic models are not predicting the correct plasma conditions for a 50 Amp hydrogen arc at 2.0 psi and 6.0 psi. Once a proper combination of these models, which allows the plasma conditions in the cascade arc to be properly modeled, is determined, the transport and finite rate kinetics models can be used in computer simulations to properly model arcjet thrusters.

Acknowledgments

The authors would like to thank Newton Wright and Fred Schwartz for their help with the experiment. The authors would also like to thank Dr. L. Montgomery Smith for guidance in data analysis. This work was supported by the Air Force Office of Scientific Research under contract #F49620-94-1-0331.

References

1. Dave King, Rocket Research Company, personal communication.
2. Keefer, D., Burtner, D., Moeller, T., and Rhodes, R., "Multiplexed Laser Induced Fluorescence and Non-equilibrium Processes in Arcjets," AIAA 94-2656, 25th AIAA Plasmadynamic and Lasers Conference, Colorado Springs, CO, June, 1994.
3. Miller, S. and Martinez-Sanchez, M., "Nonequilibrium Numerical Simulation of Radiation Cooled Arcjets," IEPC-93-218, 23rd International Electric Propulsion Conference, Seattle, WA, September, 1993.
4. Butler, G. W., Kashiwa, B. A., and King, D. Q., "Numerical Modeling of Arcjet Performance," AIAA 21st Fluid

Dynamics, Plasma Dynamics and Lasers Conference, Seattle, WA, June, 1990.

5. Megli, T.W., Krier, H., and Burton, R.L., "A Plasmadynamics Model for Nonequilibrium Processes in N_2/H_2 Arcjets," AIAA 95-1961, AIAA 26th Plasmadynamics and Lasers Conference, San Diego, CA, June, 1995.
6. Jeng, S. M., Keefer, D., Welle, R. and Peters, C., "Laser Sustained Plasmas in Forced Convection Flow, Part II: Comparison of Numerical Model With Experiment," AIAA Journal, Vol. 25, No. 9, pp. 1224-1230, September, 1987.
7. Wiese, W. L., Paquette, D. R. and Solarski, J. E., "Profiles of Stark-Broadened Balmer Lines in a Hydrogen Plasma," Phys. Rev., Vol. 129, No. 3, pp. 1225-1232, February, 1963.
8. Hargus, W., Micci, M., and Spores, R., "Interior Spectroscopic Investigation of the Propellant Energy Modes in an Arcjet Nozzle," AIAA 94-3302, 30th Joint Propulsion Conference, Indianapolis, IN, June, 1994.
9. Zube, D.M., and Auweter-Kurtz, M., "Spectroscopic Arcjet Diagnostics Under Thermal Equilibrium and Nonequilibrium Conditions," AIAA-93-1792, 29th Joint Propulsion Conference, Monterey, CA, June, 1993.
10. Rhodes, R., and Keefer, D., "Non-equilibrium Modeling of Hydrogen Arcjet Thrusters," IEPC-93-217, 23rd International Electric Propulsion Conference, Seattle, WA, September, 1993.
11. Cho, K. Y., "Non-Equilibrium Thermodynamic Models and Applications to Hydrogen Plasmas," Ph.D. Thesis, Georgia Institute of Technology, March 1988.
12. McCay, T.D. and Dexter, C.E., "Chemical Kinetic Performance Loss for a Hydrogen Laser Thermal Thruster," J. Spacecraft and Rockets, Vol. 24, No. 4, pp. 372-376, 1987.
13. Park, C., Non-equilibrium Hypersonic Aerothermodynamics, John Wiley & Sons, New York, 1990.
14. Griem, H., Plasma Spectroscopy, McGraw-Hill, 1964.
15. Griem, H., Spectral Line Broadening by Plasmas, Academic Press, New York, 1974.
16. Smith, L. M., Keefer, D., and Sudharsanan, S.I., "Abel Inversion Using Transform Techniques," J. Quant. Spectrosc. Radiat. Transfer, Vol. 39, No. 5, pp. 367-373, 1988.
17. Smith, L.M., "Nonstationary Noise Effects in the Abel Inversion", IEEE Transactions on Information Theory, Vol. 34, No. 1, pp. 158-161, Jan. 1988.

Table 1. Reaction rates for hydrogen.

	Reaction	a	n	E
1	$H + H + M \leftrightarrow H_2 + M$	$6.40e+17$	1.0	0.
2	$H^+ + e + M \leftrightarrow H + M$	$5.26e+26$	2.5	0.
3	$H_2 + e \rightarrow H + H + e$	$1.91e+11$	-1.0	-203.
4	$H^+ + e \rightarrow H + h\nu$	$3.77e+13$	0.58	0.
5	$H^+ + e + e \rightarrow H + e$	$2.19e+41$	5.06	0.
6	$H + e \rightarrow H^+ + e + e$	$1.81e+14$	0.	-244750

Where the forward reaction rate $k_f = a/T^n \exp(E/RT)$,
 $T = T_e$ for reactions 3, 5, and 6, and M is any third body:

Table 2. Comparison of Experimentally Determined Power and Electric Field With UTSI Cascade Arc Computer Simulation Results.

	Electric Field [V/cm]		Power In [W/cm]		Power Out [W/cm]	
	2.0 psi	6.0 psi	2.0 psi	6.0 psi	2.0 psi	6.0 psi
Experiment	31.5 ± 0.6	40.0 ± 0.7	1968 ± 30	2008 ± 35	$1965 \pm 278.$	$1965 \pm 278.$
Equilibrium	46.4	46.3	2320.	2317.	2264.	2267.
Nonequilibrium	101.0	69.7	5048.	3486.	4853.	3401.

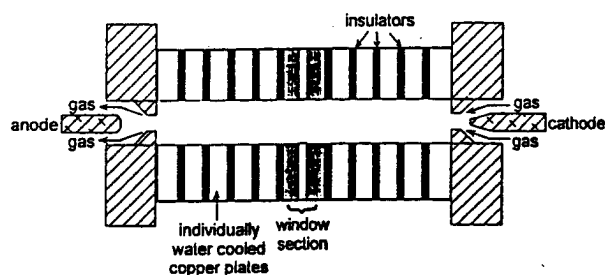


Figure 1. Cascade arc assembly.

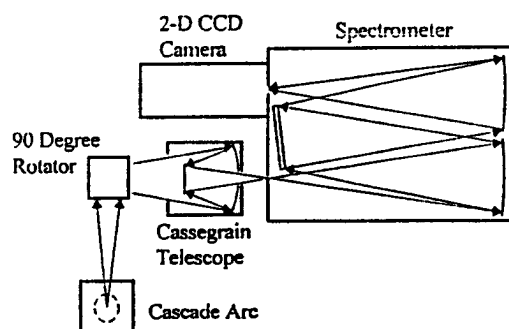


Figure 2. Cascade arc optical setup.

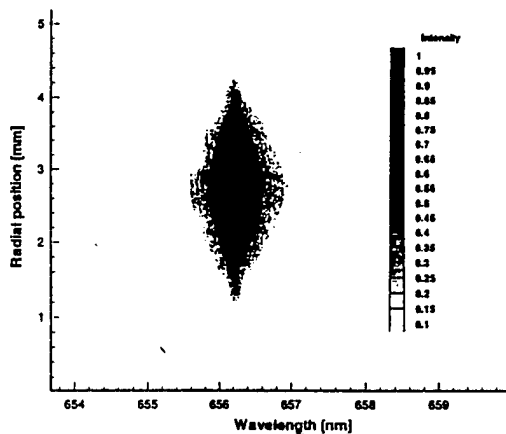


Figure 3. OMA image of the spatially resolved H_{α} line in a 50 Amp hydrogen arc at 6.0 psi. The intensity is normalized to 1.

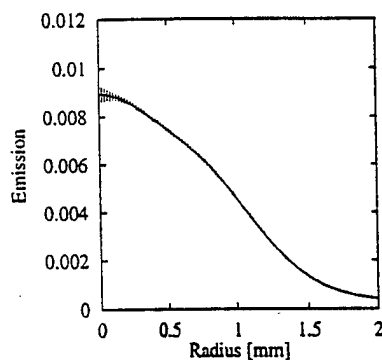


Figure 4. Radial profile of the spectral row containing the peak emission for the H_{α} line in a 50 Amp hydrogen arc at 6.0 psi. Error bars indicate uncertainty resulting from Abel inversion.

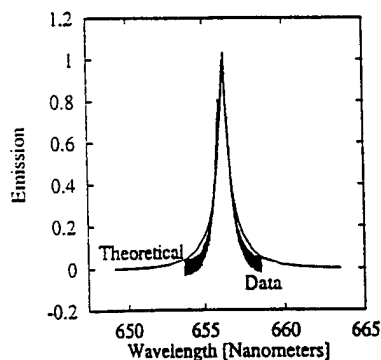


Figure 5. Measured and fitted theoretical lineshapes of H_{α} line in a 50 Amp hydrogen arc at 6.0 psi at a radius of 0.04 mm.

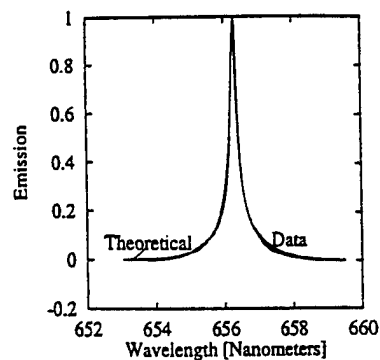


Figure 6. Measured and fitted theoretical lineshapes of H_{α} line in a 50 Amp hydrogen arc at 6.0 psi at a radius of 1.5 mm.

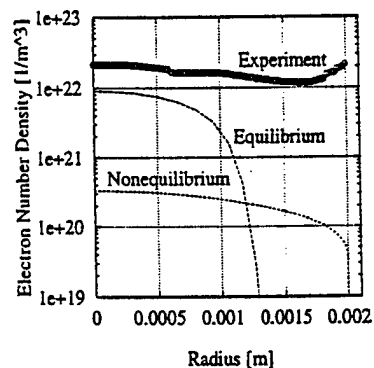


Figure 7. Comparison of experimental and numerical radial distributions of electron number density in a 50 Amp hydrogen arc at 2.0 psi.

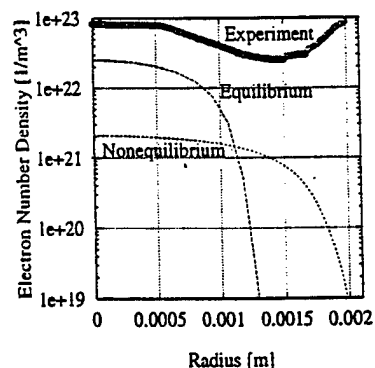


Figure 8. Comparison of experimental and numerical radial distributions of electron number density in a 50 Amp hydrogen arc at 6.0 psi.

STUDIES OF NONEQUILIBRIUM HYDROGEN/NITROGEN PLASMAS USING A CASCADE ARC

Trevor Moeller, Dennis Keefer, and Robert Rhodes
University of Tennessee Space Institute
B. H. Goethert Parkway
Tullahoma, TN 37388
(615) 393-7485

Abstract

A cascade arc facility has been constructed at UTSI to study the effect of nonequilibrium transport properties in hydrogen-nitrogen arcjet propellant plasmas. These studies will be used to guide development of the physical models required for further development of arcjet computational codes. The cascade arc has been operated on hydrogen at 50 Amps and at pressures of 13.8 kPa (2.0 psi) and 41.3 kPa (6.0 psi). Preliminary spatially resolved spectral data at these conditions have been collected for the Balmer H_{α} line. Theoretical, Stark broadened, H_{α} lineshapes have been fitted to the experimental lineshapes to determine the radial distributions of electron number density. These number densities were compared to values taken from the nonequilibrium and equilibrium cascade arc simulations. The simulations underpredict the peak experimental number densities; however, the profile of the nonequilibrium solution matches the experiment.

INTRODUCTION

Arcjets offer significant advantages for satellite station keeping and maneuvering, since their specific impulse can be more than twice that of conventional resistojets or chemical thrusters commonly used for these missions. Four commercial satellites using these new arcjet thrusters for orbit maintenance are already in use (King 1996). Current arcjet thruster performance, however, is far below the limits of an ideal arcjet, leaving room for significant improvements. Computational codes can be used to guide refinements in the basic arcjet configuration which would lead to more uniform radial temperature profiles, and a number of arcjet codes have been developed for this purpose (Keefer 1994, Miller 1993, Butler 1990). However, it is now clear that there are important nonequilibrium processes in the propellant plasma which must be understood before adequate physical models can be constructed for use in these computational codes. A cascade arc facility has been constructed at UTSI which permits measurements of nonequilibrium transport properties to be made on a controlled nonequilibrium propellant plasma to guide development of the physical models required for further development of the computational codes.

REASONS FOR UTILIZING A CASCADE ARC RATHER THAN AN ARCJET

Some of the most important chemical and transport processes in an arcjet arc, e.g. radial species diffusion and recombination, occur on time scales that are comparable to the convective times in an arcjet. This fast convection produces the strong axial gradients found in an arcjet plasma. Therefore, the plasma conditions at a given point in an arcjet depend strongly on the previous history of the plasma passing through that point. Comparison of code predictions with measurements in this case requires that the entire upstream flow field be accurately predicted. Differences between measured and predicted quantities could be due to inaccuracies in the models at any point upstream of the measurement location. This makes it very difficult to assess which model mechanisms or rates should be altered to improve the code.

Cascade arcs have long been used as a means to measure the fundamental atomic constants and transport properties of high temperature gases (Weise 1963). The cascade arc has a diameter similar to that of an arcjet constrictor but the flow velocity is much smaller and the length of the arc is tens of diameters as compared to one diameter in an arcjet. This produces an arc with similar properties to an arcjet but with negligible axial gradients. The radial temperature profiles in the cascade arc are controlled primarily by diffusive transport properties rather than convection. In the cascade arc, where there are no significant axial gradients, the nonequilibrium plasma parameters are determined by a balance between radial diffusion and chemical reactions and an axially constant but radially dependent energy input. The plasma properties depend on the local conditions at the measurement station rather than a complex convolution of all the conditions upstream of the point of measurement. Differences observed

between code predictions and measured quantities are more easily related to specific reactions or diffusion rates which must be modified to improve the code models.

UTSI EQUILIBRIUM/NONEQUILIBRIUM CASCADE ARC COMPUTER CODE

The equilibrium and nonequilibrium UTSI arcjet computer codes have been modified into one-dimensional nonequilibrium and equilibrium Cascade Arc Plasma Simulation (CAPS) codes (Rhodes 1993). At present these codes model a H_2 , H , H^+ , e hydrogen system. Both codes include radiation transport. The nonequilibrium version has a two-temperature model for heavy species and electrons, species diffusion, and a finite rate chemistry kinetics model. In both codes it is assumed that the pressure is constant, the radial velocity is zero, and the radial current density is zero. The required mass flow is assured by adjustment of velocity levels. The consequence of these assumptions is that species production and diffusion are locally balanced and total production is balanced by wall losses for the axial momentum, energy, electron energy, and species. The transport properties for both the equilibrium and nonequilibrium versions of the UTSI cascade arc computer code are calculated using a computer code written by Cho based on the procedures developed by DeVoto (Cho 1988). The reaction rates for the hydrogen system used in the computer simulations presented in this paper are shown in Table 1. The "slow" and "fast" rates, presented at the 25th AIAA Plasmadynamics and Lasers Conference (Keefer 1994), have different chemical kinetic rates for the three-body ionization and recombination of hydrogen atoms by electrons. The forward reaction rates in Table 1 are given by $k_f = a/T^n \exp(E/RT)$. T is the electron temperature for reactions 3, 5, 5r, and 5i; and M is any third body. Reaction 5r is the slow recombination rate, and 5i is the slow ionization rate.

TABLE 1. Reaction Rates for Hydrogen.

	Reaction	a	n	E
1	$H + H + M \leftrightarrow H_2 + M$	6.40e+17	1.0	0.
2	$H^+ + e + M \leftrightarrow H + M$	5.26e+26	2.5	0.
3	$H_2 + e \rightarrow H + H + e$	1.91e+11	-1.0	-203.
4	$H^+ + e \rightarrow H + h\nu$	3.77e+13	0.58	0.
5	fast rates			
	$H^+ + e + e \leftrightarrow H + e$	7.08e+39	4.5	0.
5r	slow rates			
	$H^+ + e + e \rightarrow H + e$	2.19e+41	5.06	0.
5i	$H + e \rightarrow H^+ + e + e$	1.81e+14	0.	-244750

UTSI CASCADE ARC FACILITY

The UTSI cascade arc is comprised of individually water cooled copper plates separated by electrical insulators (Figure 1). These plates are 3.175 mm (1/8 ") thick and form a 4 mm diameter arc channel that is approximately 40 mm long. The insulators are ceramic paper or mica 0.254 mm (0.010") thick. A modified plate with windows allows optical access. This section is located in the center of the cascade arc to minimize end effects. The cathode is a 6.35 mm (0.250") diameter thoriated tungsten rod with a 60 degree cone on the end. The anode is 9.144 mm (0.360") diameter thoriated tungsten rod with a blunt end. Both electrodes are cooled by a water jet impinging on their back surface. The arc is driven by a 50 Amp, 600 V power supply. A cascaded centrifugal pump delivers 41.64 liters/min (11 gal/min) of water at 1.38 MPa (200 psi) to cool the copper plates and electrodes. The cascade arc is positioned vertically to eliminate arc asymmetries caused by buoyancy.

Accurate measurement of plasma parameters requires careful integration of the external optics with the design of the central window section. Abel inversion of the emission data is needed to provide radial measurements of the plasma properties (Griem 1964). Absolute emission measurements are necessary to determine species concentrations and provide a more accurate measurement of plasma temperatures. Absolute calibration will be performed using traceable calibration lamps. Since the lamp cannot be placed within the cascade structure, this requires that the limiting aperture is not at the cascade disk or external optics, but is determined by the internal optics of the spectrometer. To provide a small entrance solid angle for the cascade window section and to avoid off-

axis aberrations, an adjustable, reflective cassegrain optical collection system is used. This collects light from the arc and directs it into a 1.25 meter focal length spectrometer so that the primary mirror in the spectrometer is overfilled. Before entering the cassegrain telescope the light from the arc is rotated ninety degrees so that the radial dimension of the arc image lies along the slit. A two-dimensional optical multichannel analyzer (OMA) with image intensifier is used to collect and digitize the data. This detector has a 512 x 512 pixel detector array with 19 μm pixel spacing and is used to simultaneously acquire spectral data at many radial locations. The magnification of the optical system is approximately 1.0 giving 200 pixels across the 4 mm diameter arc channel. Further details of the experimental setup were presented at the 32th Joint Propulsion Conference (Moeller 1996).

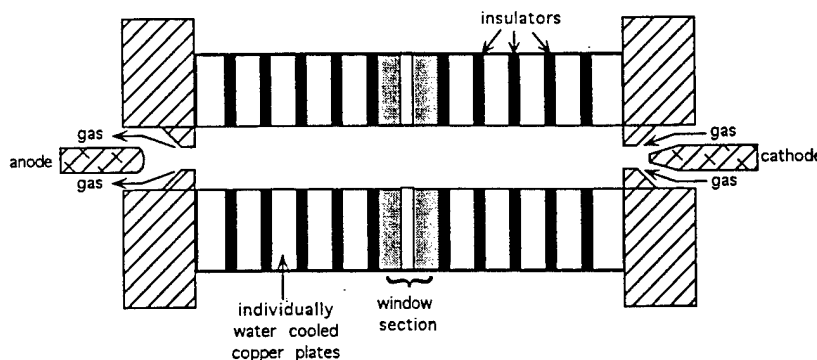


FIGURE 1. Cascade Arc Assembly.

COMPARISON OF NUMERICAL AND EXPERIMENTAL RESULTS

The cascade arc was operated with pure hydrogen arcs at 13.8 kPa (2.0 psi) and 41.3 kPa (6.0 psi) and a current of 50 A. Preliminary spectral emission data from the 656.28 nm Balmer alpha, H_{α} , line were collected using a 1.25 m Spex Monochromator and a two-dimensional OMA detector (Moeller 1996). Ten images of the arc were collected at each pressure. The OMA detector exposure times were 8.0 seconds for the 41.3 kPa case and 14.0 seconds for the 13.8 kPa case. The 13.8 kPa case requires longer exposure times because the intensity of the radiation is lower for this smaller pressure. The images of the arc have 512 spectral pixels and 256 spatial pixels. Wavelength calibration was performed on the spectral pixels using seven lines from a low density neon calibration source. The spatial pixels were calibrated by taking images of a 50 μm vertical slit backlit by a continuous source and placed in the same position as the arc when the cascade is in operation. By moving the vertical slit across the location of the arc with a translation table, the spatial pixels were associated with a radial position across the arc region. The spectrometer slit function was both spectrally and spatially deconvolved from the intensity using Wiener filters (Gonzalez 1977). Further details of the experimental procedure were presented at the 32nd Joint Propulsion Conference (Moeller 1996). Abel inversion using transform techniques (Smith 1988) provided spatially resolved emission coefficient line profiles. Electron density was determined by fitting theoretical Stark broadened line profiles to the experimentally measured emission coefficient line profiles. Figure 2 shows a comparison of the theoretical Stark profile with the experimental data for the 41.3 kPa case at a radius of 1.5 mm. The fit at this radius is typical of those at other radii.

Comparisons of the radial distribution of calculated and experimental electron number densities for the 13.8 kPa and 41.3 kPa cases are presented in Figures 3 and 4, respectively. The simulations were run using the two sets of finite chemical kinetic rates (Table 1). The error bars on the experimental electron number densities (Figures 3 and 4) are plus or minus one standard deviation of the ten realizations at each pressure. At both pressures the nonequilibrium and equilibrium computer simulations underpredict the experimentally determined electron number densities for all radii and for both the "fast" and "slow" ionization rates. While the electron number densities are underpredicted by almost two orders of magnitude for the "slow" cases, the results for the "fast" case reduce this underprediction to about a factor of four. The "fast" and "slow" simulations both assume a catalytic wall at which recombination of electrons and ions is complete. Even though the equilibrium simulations predict the peak electron number density better than the nonequilibrium simulations, the nonequilibrium distribution has nearly the same profile as the experimental data. The distribution labeled "fast" reflective wall is a simulation with "fast" finite rate

chemical kinetics and a reflective wall model in which plasma species reflect off of the wall. This case results in more electrons near the wall and predicts the experimental distribution better than the catalytic wall. An interesting feature of the experimental number density profiles is the positive slope of the curve close to the wall of the arc channel at 2 mm. This feature appears to be the result of relatively poor fits of theoretical Stark line profiles to the noisy data and a low signal-to-noise ratio in the regions near the wall.

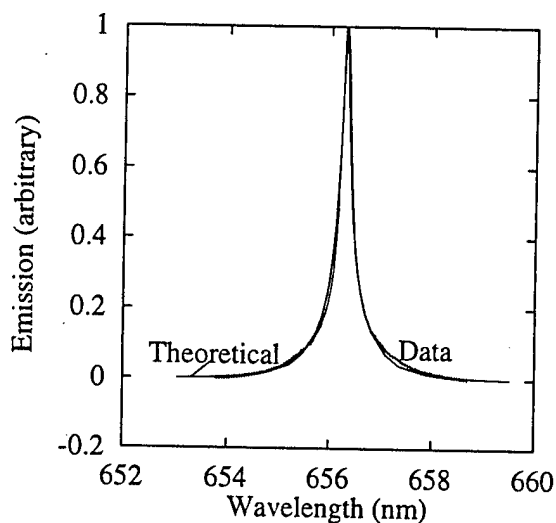


FIGURE 2. Measured and Fitted Theoretical Lineshapes of H_{α} Line in a 50 Amp Hydrogen Arc at 41.3 kPa at a Radius of 0.04 mm.

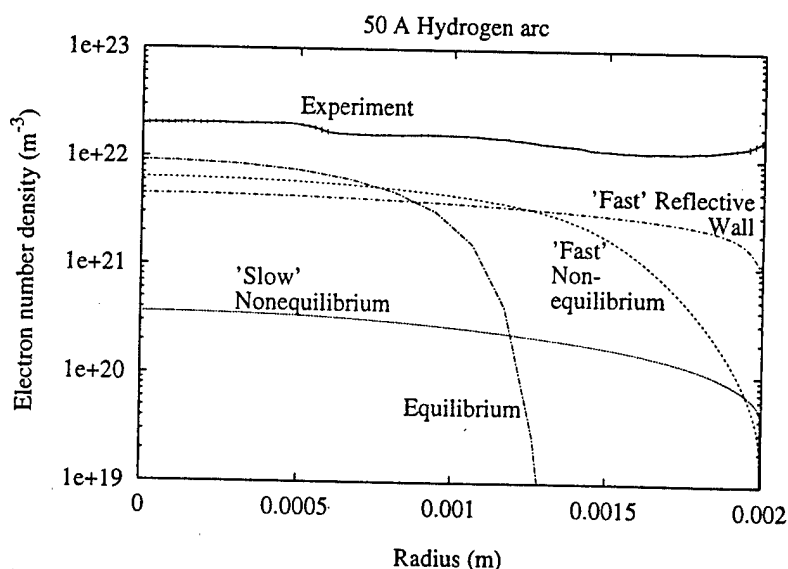


FIGURE 3. Comparison of Experimental and Numerical Radial Distributions of Electron Number Density in a 50 Amp Hydrogen Arc at 13.8 kPa (2.0 psi). "Fast" and "slow" represent nonequilibrium computer simulations using two different chemical kinetic rates for the ionization of hydrogen due to electrons. Reflective wall indicates solution in which plasma species reflect off of wall.

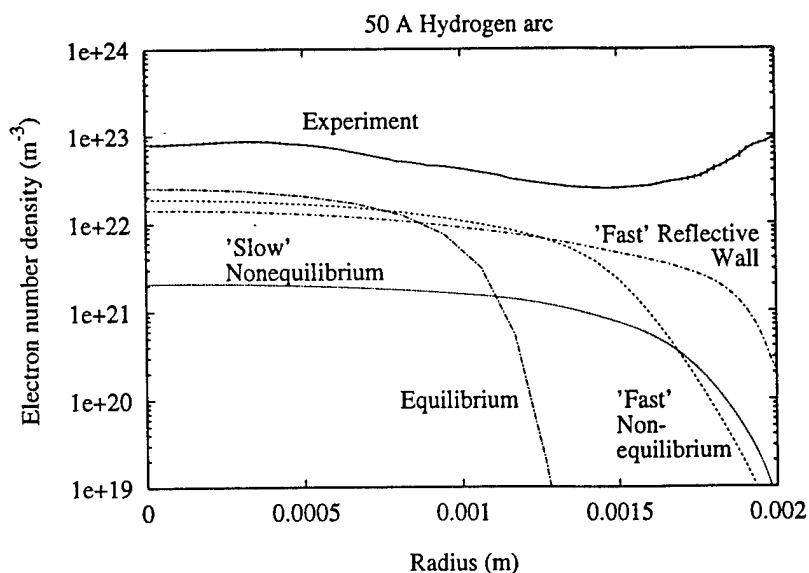


FIGURE 4. Comparison of Experimental and Numerical Radial Distributions of Electron Number Density in a 50 Amp Hydrogen Arc at 41.3 kPa (6.0 psi). "Fast" and "slow" represent nonequilibrium computer simulations using two different chemical kinetic rates for the ionization of hydrogen due to electrons. Reflective wall indicates solution in which plasma species reflect off of wall.

Table 2 is a comparison of the experimental and numerical electric field for the 13.8 kPa and 41.3 kPa cases. The experimental electric fields were determined by finding the slope of the best fit line through the potentials of the cascade plates. The electric fields from the equilibrium simulations overpredict the experimentally determined values by 50 percent for the 13.8 kPa case and 15 percent for the 41.3 kPa case. These overpredictions increase to 220 percent and 75 percent for the "slow" nonequilibrium simulations at 13.8 kPa and 41.3 kPa, respectively. The overpredictions of the electric field for the "fast" nonequilibrium simulations are 81 percent for 13.8 kPa and 48 percent for 41.3 kPa. It is evident that the chemical kinetic rates have a large impact on the electric field realized in the nonequilibrium computer simulations. The "fast" reflective wall solution overpredicts the electric field by 56 percent and 26 percent, respectively.

TABLE 2. Comparison of Experimentally Determined Electric Field (V/cm) with UTSI Cascade Arc Plasma Simulation (CAPS) Code Values.

	Equilibrium Simulation	"Slow" Nonequilibrium	"Fast" Nonequilibrium	"Fast" Reflective Wall	Experiment
Case 1: 13.8 kPa	46.4	101.0	57.2	49.1	31.5 ± 0.6
Case 2: 41.3 kPa	46.3	69.7	59.1	50.4	40.0 ± 0.7

CONCLUSIONS

It can be shown that the electric field is directly proportional to electron collision frequency and inversely proportional to electron number density. Comparisons of the computer simulations with experimental results show that the electron number densities are underpredicted to a greater degree than the simulations overpredict the electric field. This suggests that the computer predicted electron collision frequencies, as well as the electron number densities, are in error. Therefore, neither the nonequilibrium transport properties nor the chemical kinetic rates appear to be modeled properly.

In the analysis of the nonequilibrium hydrogen plasma performed to date, only the electron density was measured. The spatial distribution of the other atomic and molecular species were not measured, and in the simulation were determined by the rate constants given in Table 1. Evaluation of the other reaction rates will require measurement of these other species. Combined emission and laser induced fluorescence measurements will provide a detailed specification of species and temperatures as a function of radius. Current and voltage measurements will provide an accurate measurement of the Ohmic power per unit length deposited in the arc to be used for a global validation of the simulations. Nonequilibrium plasma models will be validated through comparison of the experimental measurements with computer simulations of the arc which use the candidate models.

Acknowledgments

The authors would like to thank Newton Wright and Fred Schwartz for their help with the experiment. The authors would also like to thank Dr. L. Montgomery Smith for guidance in data analysis. This work was supported by the Air Force Office of Scientific Research under contract #F49620-94-1-0331 and the National Science Foundation under NSF Grant # CTS-9512489.

References

- Butler, G. W., B. A. Kashiwa, and D. Q. King (1990) "Numerical Modeling of Arcjet Performance," AIAA 90-1474, AIAA 21st Fluid Dynamics, Plasma Dynamics and Lasers Conference, Seattle, WA, June, 1990.
- Cho, K. Y. (1988) "Non-Equilibrium Thermodynamic Models and Applications to Hydrogen Plasmas," Ph.D. Thesis, Georgia Institute of Technology, March 1988.
- Gonzalez, Rafael, and Paul Wintz (1977) *Digital Image Processing*, Addison-Wesley Publishing, Ontario, 1977.
- Griem, H. (1964) *Plasma Spectroscopy*, McGraw-Hill, 1964.
- Keefer, D., D. Burtner, T. Moeller, and R. Rhodes (1994) "Multiplexed Laser Induced Fluorescence and Non-equilibrium Processes in Arcjets," AIAA 94-2656, 25th AIAA Plasmadynamic and Lasers Conference, Colorado Springs, CO, June, 1994.
- King, Dave (1996) Personal Communication, Rocket Research Corporation, Redmond, Washington, January 1996.
- Miller, S. and M. Martinez-Sanchez (1993) "Nonequilibrium Numerical Simulation of Radiation Cooled Arcjets," IEPC-93-218, *Proceedings of the 23rd International Electric Propulsion Conference*, 3: 2032-2050, Published at The Ohio State University, Columbus OH, 1993.
- Moeller, T., D. Keefer, and R. Rhodes (1996) "Cascade Arc Studies of Nonequilibrium Hydrogen Plasmas," AIAA 96-3294, 32nd AIAA/ASME/SAE/ASEE Joint Propulsion Conference, Lake Buena Vista, FL, July 1-3, 1996.
- Rhodes, R., and D. Keefer (1993) "Non-equilibrium Modeling of Hydrogen Arcjet Thrusters," IEPC-93-217, *Proceedings of The 23rd International Electric Propulsion Conference*, 3: 2020-2031, Published at The Ohio State University, Columbus, OH, 1993.
- Smith, L. M., D. Keefer, and S.I. Sudharsanan (1988) "Abel Inversion Using Transform Techniques," *J. Quant. Spectrosc. Radiat. Transfer*, 39:367-373.
- Wiese, W. L., D. R. Paquette, and J. E. Solarzski (1963) "Profiles of Stark-Broadened Balmer Lines in a Hydrogen Plasma," *Phys. Rev.*, 129:1225-1232, February, 1963.



IEPC 97-063

**NONEQUILIBRIUM HYDROGEN/NITROGEN
PLASMAS STUDIES USING A CASCADE ARC**

Trevor Moeller, Dennis Keefer, and Robert Rhodes

University of Tennessee Space Institute

B. H. Goethert Parkway

Tullahoma, TN 37388

**25th International Electric Propulsion Conference
August 24-28, 1997, Cleveland, Ohio**

NONEQUILIBRIUM HYDROGEN/NITROGEN PLASMAS STUDIES USING A CASCADE ARC

Trevor Moeller, Dennis Keefer, and Robert Rhodes
University of Tennessee Space Institute
B. H. Goethert Parkway
Tullahoma, TN 37388

ABSTRACT

A cascade arc facility has been constructed at The University of Tennessee Space Institute (UTSI) to study the effect of nonequilibrium transport properties in hydrogen-nitrogen arcjet propellant plasmas. These studies are being used to guide development of the physical models required for further development of arcjet computational codes. The cascade arc has been operated on hydrogen with a current of 50 A at pressures of 2.0 psi and 6.0 psi. Spatially resolved spectral data at these conditions have been collected for the Balmer H_{α} , H_{β} , H_{γ} , and H_{δ} lines. The experimental H_{α} lineshapes have been fitted to theoretical, Stark broadened, H_{α} lineshapes to determine the radial distributions of electron number density. Radial profiles of an equilibrium plasma temperature have also been estimated from Boltzmann plots using the line emission from H_{α} , H_{β} , H_{γ} , and H_{δ} lines. The electron number densities and plasma temperatures were compared to values predicted by nonequilibrium and equilibrium cascade arc simulations using the UTSI Cascade Arc Plasma Simulation (CAPS) code. The nonequilibrium computer simulations were run using three different sets of finite rate chemical kinetics. By varying finite rate chemical kinetics in the nonequilibrium simulation code, the experimental electric field has been predicted. The nonequilibrium simulations underpredict the peak experimental number densities between 30 percent and 1.5 orders of magnitude. The peak plasma temperature is overpredicted by the simulations by as much as a factor of two. In general, however, the radial profiles of the nonequilibrium solutions better match the experimental measurements.

INTRODUCTION

Electric propulsion thrusters offer significant advantages for satellite station keeping and

maneuvering, since their specific impulse can be more than twice that of conventional resistojets or chemical thrusters commonly used for these missions. Computational codes can be used to guide refinements in the configuration of electric propulsion thrusters which lead to better thruster performance, and a number of these codes have been developed for this purpose¹⁻⁴. However, it is now clear that there are important nonequilibrium processes in the propellant plasma which must be understood before adequate physical models can be constructed for use in these computational codes. A cascade arc facility has been constructed at The University of Tennessee Space Institute (UTSI) which permits diagnostic measurements to be made on a controlled nonequilibrium propellant plasma to evaluate the kinetic models and transport properties required for further development of the computational codes.

REASONS FOR UTILIZING A CASCADE ARC RATHER THAN AN ELECTRIC PROPULSION THRUSTER

Some of the most important chemical and transport processes in the propellant plasmas of electric propulsion thrusters, e.g. radial species diffusion and recombination, occur on time scales that are comparable to the convection times in these thrusters. This fast convection produces the strong axial gradients found in the propellant plasma. Therefore, the plasma conditions at a given point in a thruster depend strongly on the previous history of the plasma passing through that point. Comparison of code predictions with measurements in this case requires that the entire upstream flow field be accurately predicted. Differences between measured and predicted quantities could be due to inaccuracies in the models at any point upstream of the measurement location. This makes it very difficult to assess which model mechanisms or rates should be altered to improve the code.

*Copyright 1997 by the Electric Rocket Propulsion Society. All rights reserved.

Cascade arcs have long been used as a means to measure the fundamental atomic constants and transport properties of high temperature gases⁵. The cascade arc has a flow velocity much smaller than seen in electric propulsion thrusters, and the length of the arc plasma in the cascade is tens of diameters as compared to one diameter in typical electric propulsion devices. This produces plasmas with properties similar to propellant plasmas in electric propulsion thrusters but with negligible axial gradients. The radial temperature profiles in the cascade arc are controlled primarily by diffusive transport properties rather than convection as seen in electric propulsion thrusters. In the cascade arc, where there are no significant axial gradients, the nonequilibrium plasma parameters are determined by a balance between radial diffusion and chemical reactions and an axially constant but radially dependent energy input. The plasma properties depend on the local conditions at the measurement station rather than a complex time-space convolution of all the conditions upstream of the point of measurement. Differences observed between code predictions and measured quantities are more easily related to the specific reactions or diffusion rates which must be modified to improve the code models.

UTSI EQUILIBRIUM/NONEQUILIBRIUM CASCADE ARC COMPUTER CODE

The equilibrium and nonequilibrium UTSI arcjet computer codes have been modified into one-dimensional nonequilibrium and equilibrium Cascade Arc Plasma Simulation (CAPS) codes⁶. At present these codes model a H_2 , H , H^+ , e hydrogen system. Both codes include radiation transport. The nonequilibrium version includes species diffusion and a finite rate chemistry kinetics model and uses a two-temperature model with separate energy equations for heavy species and electrons. In both codes it is assumed that the pressure is constant, the radial velocity is zero, and the radial current density is zero. The required mass flow is assured by adjustment of velocity levels. The consequence of these assumptions is that species production and diffusion are locally balanced and total production is balanced by wall losses for the axial momentum, energy, electron energy, and species. The transport properties for both the equilibrium and nonequilibrium versions of the UTSI cascade arc computer code are calculated using a computer code written by Cho based on the procedures developed by DeVoto⁷. The reaction rates for the hydrogen system used in the computer simulations presented in this

paper are shown in Table 1. The "slow" and "fast" rates, presented at the 25th AIAA Plasmadynamics and Lasers Conference², have different chemical kinetic rates for the three-body ionization and recombination of hydrogen atoms by electrons. The "U of I" (University of Illinois) rates presented at the 26th AIAA Plasmadynamics and Lasers Conference¹ are the same as the "fast" rates but have a different rate for the dissociation of molecular hydrogen by electrons⁸. The forward reaction rates in Table 1 are given by $k_f = a/T^n \exp(E/RT)$. T is the electron temperature for reactions 3, 3 U of I, 5, 5r, and 5i; and M is any third body. Reaction 5r is the slow recombination rate, and 5i is the slow ionization rate.

UTSI CASCADE ARC FACILITY

The UTSI cascade arc is comprised of individually water cooled copper plates separated by electrical insulators (Figure 1). These plates are 3.175 mm (1/8") thick and form a 4 mm diameter arc channel that is approximately 40 mm long. The insulators are ceramic paper or mica 0.254 mm (0.010") thick. A modified plate with windows allows optical access. This section is located in the center of the cascade arc to minimize end effects. The cathode is a 6.35 mm (0.250") diameter thoriated tungsten rod with a 60 degree cone on the end. The anode is 9.144 mm (0.360") diameter thoriated tungsten rod with a blunt end. Both electrodes are cooled by a water jet impinging on their back surface. The arc is driven by a 50 Amp, 600 V power supply. A cascaded centrifugal pump delivers 41.64 liters/min (11 gal/min) of water at 1.38 MPa (200 psi) to cool the copper plates and electrodes. The cascade arc is positioned vertically to eliminate arc asymmetries caused by buoyancy.

Accurate measurement of plasma parameters requires careful integration of the external optics with the design of the central window section. Abel inversion of the emission data is needed to provide radial measurements of the plasma properties⁹. Absolute emission measurements are necessary to determine species concentrations and provide a more accurate measurement of plasma temperatures. To provide a small entrance solid angle for the cascade window section and to avoid off-axis aberrations, an adjustable, reflective Cassegrain optical collection system is used. This collects light from the arc and directs it into a 1.25 meter focal length spectrometer so that the primary mirror in the spectrometer is overfilled. Before entering the Cassegrain telescope the arc image is rotated ninety degrees so that the

radial dimension of the arc image lies along the slit. A two-dimensional optical multichannel analyzer (OMA) with image intensifier is used to collect and digitize the data. This detector has a 512 x 512 pixel detector array with 19 μm pixel spacing and is used to simultaneously acquire spectral data at many radial locations. The magnification of the optical system is approximately 1.0 giving 200 pixels across the 4 mm diameter arc channel. Further details of the experimental setup were presented at the 32nd Joint Propulsion Conference¹⁰.

COMPARISON OF NUMERICAL AND EXPERIMENTAL RESULTS

The cascade arc was operated with pure hydrogen arcs at 2.0 psi and 6.0 psi and a current of 50 A. Spectral emission data from the 656.28 nm Balmer alpha, H_{α} , line in the 8th order were collected using a 1.25 m Spex spectrometer with a 316 groove/mm echelle grating and a two-dimensional OMA detector¹⁰. Six images of the arc were collected at each pressure. A 1.9 N.D. filter and a 550 nm high pass filter were utilized to prevent detector saturation and eliminate interference from higher order lines, respectively. The OMA detector exposure times were 0.2 seconds for the 6.0 psi case and 2.0 seconds for the 2.0 psi case. The 2.0 psi case required longer exposure times because the intensity of the radiation was lower for this smaller pressure. The images of the arc have 512 spectral pixels and 400 spatial pixels. Wavelength calibration was performed on the spectral pixels using seven lines from a low density neon calibration source. The spatial pixels were calibrated by taking images of a 50 μm vertical slit backlit by the neon lamp and placed in the same position as the arc when the cascade is in operation. By moving the vertical slit across the location of the arc with a translation table, the spatial pixels were associated with a radial position across the arc region. The spectrometer slit function was spectrally deconvolved from the intensity using a digital Wiener filter¹¹. Further details of the experimental procedure were presented at the 32nd Joint Propulsion Conference¹⁰ and the 1st Conference on Synergistic Power and Propulsion Systems Technology¹². Abel inversion of the spatially resolved line intensity using transform techniques¹³ provided spatially resolved emission coefficient line profiles. Electron density was determined by fitting theoretical Stark broadened line profiles¹⁴ to the experimentally measured emission coefficient line profiles. This experiment has been repeated for

simulated ammonia and simulated hydrazine at pressures of 2 psi, 6 psi, and 10 psi. Detector exposure times of 2 seconds were used for these measurements.

To obtain estimates of equilibrium plasma temperature distributions in the 50 A hydrogen arcs at 2 psi and 6 psi, emission profiles of the H_{α} , H_{β} , H_{γ} , and H_{δ} lines were used to make radially resolved Boltzmann plots. The emission profiles were obtained using the Abel inversion technique described above. This data was collected in the second order to guarantee an accurate estimate of the continuum. A standard tungsten filament lamp was used to calibrate the spectral sensitivity of the detector over the range defined by these spectral lines.

RESULTS FOR HYDROGEN PLASMA

Comparisons of the radial distribution of calculated and experimental electron number densities for the 2.0 psi and 6.0 psi cases are presented in Figures 2 and 3, respectively. Results from experiments carried out on two different days are depicted in these figures. The simulations were run using the three sets of finite chemical kinetic rates (Table 1). The error bars on the experimental electron number densities (Figures 2 and 3) are plus or minus one standard deviation of the six realizations at each pressure. At both pressures the nonequilibrium computer simulations underpredict the experimentally determined electron number densities for all radii and for all ionization rates. While the electron number densities are underpredicted by about 1.5 orders of magnitude for the "slow" cases, the results for the "fast" case reduce this underprediction to about a factor of approximately two. The "U of I" case gives the best nonequilibrium solution results; it underpredicts the experimental values by less than an order of magnitude. Like the "U of I" case, the other nonequilibrium distributions have nearly the same profile as the experimental data. The distribution labeled "Ref" is a simulation with "fast" finite rate chemical kinetics and a reflective wall model in which plasma species reflect off of the wall. This case results in more electrons near the wall and predicts the experimental distribution better than the catalytic wall with the same kinetics.

Figure 4 shows a theoretically Stark broadened H_{α} profile fitted to 6 psi hydrogen arc data at a radius of 1.5 mm. This fit is typical of the those at other

radii. The overprediction of the wings leads to a relatively poor fit, and may be causing the experimental electron number densities to appear larger than they are in reality. Because it is likely that Doppler effects are contributing to the line broadening, the data is better represented by a Voigt profile. Figure 5 shows a Voigt profile fit to the same data in Figure 4. At the writing of this paper, electron number density profiles have not yet been determined using the Voigt line fits, though a significant decrease in the measured electron number densities is anticipated.

Figures 6 and 7 show comparisons of the radial distribution of calculated and experimental temperatures for the 2.0 psi and 6.0 psi cases, respectively. Only the "U of I" nonequilibrium solutions are presented in these plots for the sake of brevity. The computer simulations overpredict the experimental centerline temperatures by approximately 60 percent for the 2.0 psi case and match the experiment (within experimental error) for the 6.0 psi case. The measured temperature profiles do not match any of simulation temperature distributions. The negative temperature gradient at the constrictor wall and the 50 percent error of the experimental temperature distributions make these preliminary data questionable. The error bars on the experimental data are plus or minus one standard deviation calculated from the uncertainty associated with the slope of the line in the Boltzmann plot (the Boltzmann plot of a 6 psi hydrogen arc is shown in Figure 8). The relatively large error in temperature results from poor fits through the four data points in the Boltzmann plots.

Table 2 is a comparison of the experimental and numerical electric field for the 2.0 psi and 6.0 psi cases. The experimental electric fields were determined by finding the slope of the best fit line through the potentials of the cascade plates. The electric fields from the equilibrium simulations overpredict the experimentally determined values by 33 percent for the 2.0 psi case and 10 percent for the 6.0 psi case. These overpredictions increase to 180 percent and 51 percent for the "slow" nonequilibrium simulations at 2.0 psi and 6.0 psi, respectively. The electric field for the "fast" nonequilibrium simulations overpredicts the experiment by 17 percent for 2.0 psi and agrees with the value for 6.0 psi. The "fast" reflective wall solution agrees with the experiment at 2 psi and underpredicts the 6 psi value by 16 percent. The

"U of I" nonequilibrium simulations best predict the electric field, splitting the experimental values for the 2.0 psi case and matching the values for the 6.0 psi case. It is evident that the chemical kinetic rates have a large impact on the electric field realized in the nonequilibrium computer simulations.

RESULTS FOR HYDROGEN/NITROGEN PLASMAS

The radial distribution of experimental electron number densities for simulated ammonia and simulated hydrazine are shown in Figures 9 and 10, respectively. These preliminary data show an increase in electron density with pressure, and a very slight increase in electron density for the hydrazine over the ammonia. An interesting feature of the profiles is the positive slope of the curve close to the wall of the arc channel at 2 mm. This feature appears to be the result of relatively poor fits of theoretical Stark line profiles to the noisy data. Filtering of the signal noise for the mixture data has not yet been optimized and may be causing this problem. Table 3 shows a comparison of experimentally determined electric fields for the hydrogen and hydrogen/nitrogen mixtures. The electric field increases with pressure and decreases as more nitrogen is added.

CONCLUSIONS

The predicted hydrogen plasma electron number densities from all of the nonequilibrium computer simulations of the hydrogen cascade arc at 2.0 psi and 6.0 psi underpredict the experimental values by as much as 1.5 orders of magnitude. The peak electron densities are bounded by the equilibrium and the nonequilibrium solutions for the 2.0 psi case, while all of the computer simulations underpredict the peak value for 6.0 psi. Initial fits with Voigt profiles show significant contributions to line broadening that will likely lower the experimental number densities and reduce differences between the experiment and the computer simulations. The experimental electric fields have been bound by nonequilibrium computer simulations using different finite rate chemical kinetics. The "U of I" finite rate chemical kinetics matches the experimental electric field and best predicts the distribution of electron number densities. In addition to obtaining distributions of electron number densities, Boltzmann plots have been used to determine a rough estimate for the

radial distribution of plasma temperature. These preliminary experimental temperature data are overpredicted by the simulations by as much as 2.5 times.

Preliminary electron number density profiles for simulated ammonia and simulated hydrazine have been obtained for 50 Amp arcs at 2 psi, 6 psi, and 10 psi. A hydrogen/nitrogen mixture version of the CAPS code should be available shortly allowing comparisons with the experimental mixture data to commence.

ACKNOWLEDGMENTS

The authors would like to thank Newton Wright, Fred Schwartz, and Nancy O'Brien for their help with the experiment. The authors would also like to thank Dr. L. Montgomery Smith and James Hornkohl for guidance in data analysis. This work was supported by the Air Force Office of Scientific Research under contract #F49620-94-1-0331 and the National Science Foundation under NSF Grant # CTS-9512489.

REFERENCES

1. T. Megli, H. Krier, and R. Burton, "A Plasmadynamics Model for Nonequilibrium Processes in N₂/H₂ Arcjets," AIAA 95-1961, 26th AIAA Plasmadynamics and Lasers Conference, San Diego, CA, June 19-22, 1995.
2. D. Keefer, D. Burtner, T. Moeller, and R. Rhodes, "Multiplexed Laser Induced Fluorescence and Non-equilibrium Processes in Arcjets," AIAA 94-2656, 25th AIAA Plasmadynamic and Lasers Conference, Colorado Springs, CO, June, 1994.
3. S. Miller, and M. Martinez-Sanchez, "Nonequilibrium Numerical Simulation of Radiation Cooled Arcjets," IEPC-93-218, *Proceedings of the 23rd International Electric Propulsion Conference*, Vol. 3: 2032-2050, Published at The Ohio State University, Columbus OH, 1993.
4. G. W. Butler, B. A. Kashiwa, and D. Q. King, "Numerical Modeling of Arcjet Performance," AIAA 90-1474, AIAA 21st Fluid Dynamics, Plasma Dynamics and Lasers Conference, Seattle, WA, June, 1990.
5. W. L. Wiese, D. R. Paquette, and J. E. Solariski, "Profiles of Stark-Broadened Balmer Lines in a Hydrogen Plasma," *Phys. Rev.*, 129:1225-1232, February, 1963.
6. R. Rhodes, and D. Keefer, "Non-equilibrium Modeling of Hydrogen Arcjet Thrusters," IEPC-93-217, *Proceedings of The 23rd International Electric Propulsion Conference*, Vol. 3: 2020-2031, Published at The Ohio State University, Columbus, OH, 1993.
7. K. Y. Cho, "Non-Equilibrium Thermodynamic Models and Applications to Hydrogen Plasmas," Ph.D. Thesis, Georgia Institute of Technology, March 1988.
8. Janev, et al, Elementary Processes in Hydrogen Helium Plasmas, Springer-Verlag, New York, 1987.
9. H. Griem, *Plasma Spectroscopy*, McGraw-Hill, 1964, pp. 129-167.
10. T. Moeller, D. Keefer, and R. Rhodes, "Cascade Arc Studies of Nonequilibrium Hydrogen Plasmas," AIAA 96-3294, 32nd AIAA/ASME/SAE/ASEE Joint Propulsion Conference, Lake Buena Vista, FL, July 1-3, 1996.
11. R. Gonzalez, and P. Wintz, *Digital Image Processing*, Addison-Wesley Publishing, Ontario, 1977, pp. 199-209.
12. T. Moeller, D. Keefer, and R. Rhodes, "Studies of Nonequilibrium Hydrogen/Nitrogen Plasmas using a Cascade Arc," AIP Conference Proceedings 387, p. 317, The Space Technology and Applications International Forum (STAIF-97), Albuquerque, NM, Jan. 1997.
13. L. M. Smith, D. Keefer, and S.I. Sudharsanan, "Abel Inversion Using Transform Techniques," *J. Quant. Spectrosc. Radiat. Transfer*, 39:367-373, 1988.
14. Griem, H. U., *Spectral Line Broadening by Plasmas*, Academic Press, New York, 1974.

Table 1. Reaction Rates for Hydrogen.

	Reaction	a	n	E
1	$H + H + M \leftrightarrow H_2 + M$	6.40e+17	1.0	0.
2	$H^+ + e + M \leftrightarrow H + M$	5.26e+26	2.5	0.
3	U of I			
U of I	$H_2 + e \rightarrow H + H + e$	1.87e-3	-3.73	0.
3	$H_2 + e \rightarrow H + H + e$	1.91e+11	-1.0	-203.
4	$H^+ + e \rightarrow H + h\nu$	3.77e+13	0.58	0.
	fast rates			
5	$H^+ + e + e \leftrightarrow H + e$	7.08e+39	4.5	0.
	slow rates			
5r	$H^+ + e + e \rightarrow H + e$	2.19e+41	5.06	0.
5i	$H + e \rightarrow H^+ + e + e$	1.81e+14	0.	-244750

Table 2. Comparison of Experimentally Determined Electric Field (V/cm) with UTSI Cascade Arc Plasma Simulation (CAPS) Code Values.

	Equilibrium Simulation	"Slow" Non-Equilibrium	"Fast" Non-Equilibrium	"Fast" Reflective Wall	"U of I" Non-Equilibrium	Experiment June 20, 1997	Experiment July 16, 1997
Case 1: 2.0 psi	46.4	95.7	42.0	36.4	33.4	36.0 ± 1.2	31.3 ± 1.5
Case 2: 6.0 psi	46.3	64.9	43.9	36.9	44.1	44.2 ± 1.2	44.2 ± 1.0

Table 3. Experimentally Determined Electric Field (V/cm) for Hydrogen and Hydrogen/Nitrogen Mixtures.

	Hydrogen July 16, 1997	Simulated Ammonia	Simulated Hydrazine
Case 1: 2.0 psi	31.3 ± 1.5	26.4 ± 0.7	26.2 ± 0.8
Case 2: 6.0 psi	44.2 ± 1.0	38.8 ± 1.1	35.1 ± 0.9

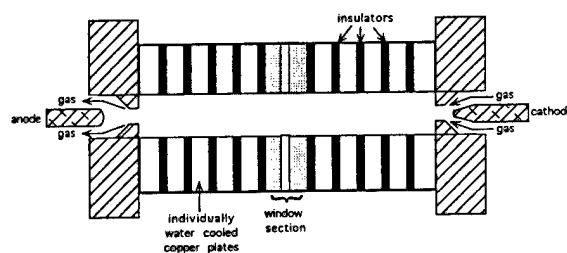


Figure 1. Cascade Arc Assembly.

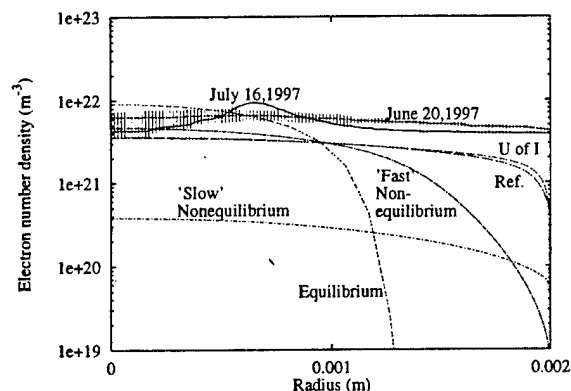


Figure 2. Comparison of Experimental and Numerical Radial Distributions of Electron Number Density in a 50 Amp Hydrogen Arc at 2.0 psi. "Fast" and "slow" represent nonequilibrium computer simulations using two different chemical kinetic rates for the ionization of hydrogen due to electrons. "U of I" indicates a finite rate solution using a different rate for the dissociation of hydrogen by electrons. "Ref" has a reflective wall boundary condition.

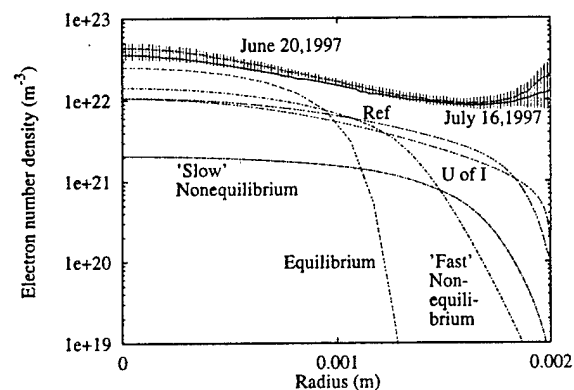


Figure 3. Comparison of Experimental and Numerical Radial Distributions of Electron Number Density in a 50 Amp Hydrogen Arc at 6.0 psi. "Fast" and "slow" represent nonequilibrium computer simulations using two different chemical kinetic rates for the ionization of hydrogen due to electrons. "U of I" indicates a finite rate solution using a different rate for the dissociation of hydrogen by electrons. "Ref" has a reflective wall boundary condition.

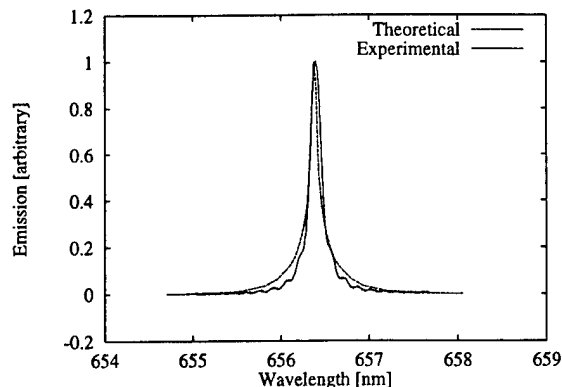


Figure 4. Measured and Fitted Theoretical Stark Lineshapes of H_{α} Line in a 50 Amp Hydrogen Arc at 6.0 psi at a Radius of 1.5 mm.

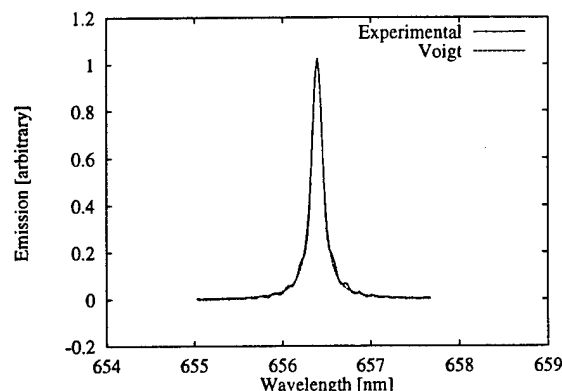


Figure 5. Measured and Fitted Theoretical Voigt Lineshapes of H_{α} Line in a 50 Amp Hydrogen Arc at 6.0 psi at a Radius of 1.5 mm.

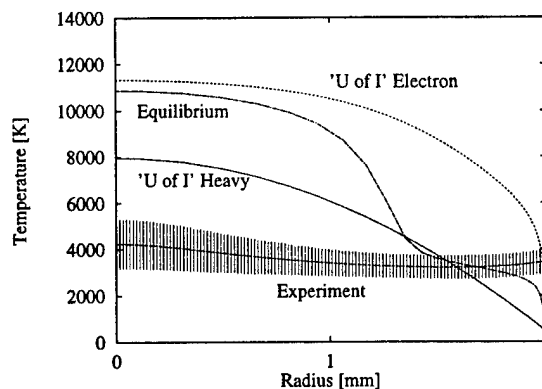


Figure 6. Comparison of Experimental and Numerical Radial Distributions of the Plasma Temperature in a 50 Amp Hydrogen Arc at 2.0 psi. "U of I" indicates a finite rate solution using "U of I" kinetics.

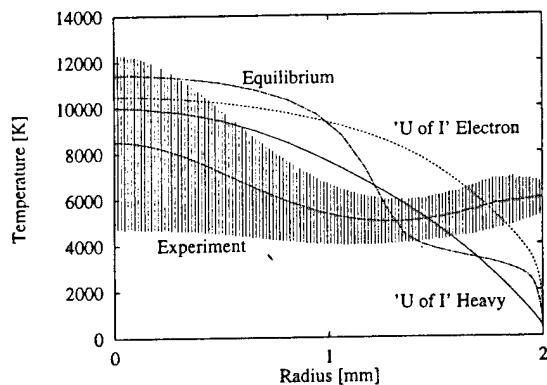


Figure 7. Comparison of Experimental and Numerical Radial Distributions of the Plasma Temperature in a 50 Amp Hydrogen Arc at 6.0 psi. "U of I" indicates a finite rate solution using "U of I" kinetics.

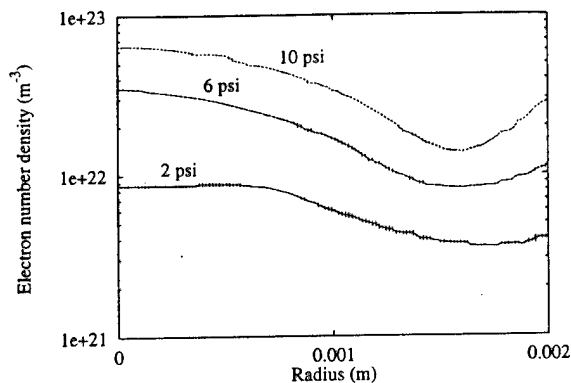


Figure 10. Radial Distributions of Electron Number Densities for Simulated Hydrazine (N_2H_4) at 2.0 psi, 6.0 psi, and 10.0 psi.

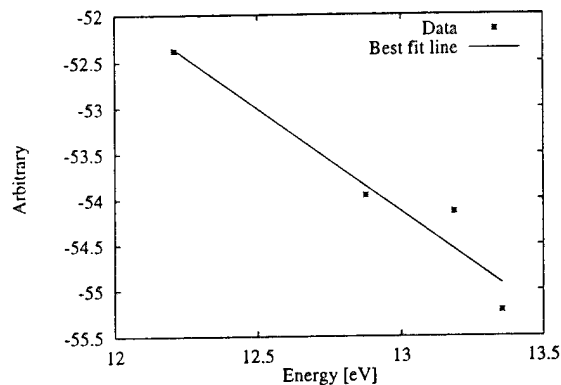


Figure 8. Boltzmann Plot Using the H_α , H_β , H_γ , and H_δ Lines in a 50 Amp Hydrogen Arc at 6.0 psi at a Radius of 1.5 mm.

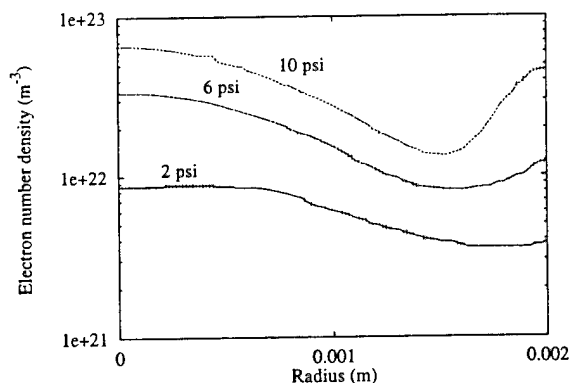


Figure 9. Radial Distributions of Electron Number Densities for Simulated Ammonia (NH_3) at 2.0 psi, 6.0 psi, and 10.0 psi.

Approved for public release,
distribution is unlimited.

AFSC

Reviewed and is
190-12